Impact of the fabrication process on the lateral–torsional buckling of welded I-section beams

Maxime Lebastard, Maël Couchaux, Alain Bureau, Mohammed Hjiaj

Impact of the fabrication process on the lateral-torsional buckling of welded I-section beams

Maxime Lebastard[a,b], Maël Couchaux[b], Alain Bureau[a], Mohammed Hjiaj[b].

[a]: Centre Technique Industriel de la Construction Métallique, Espace technologique – L'Orme des Merisiers – Immeuble Apollo, 91190 Saint-Aubin, France

[b]: Institut National des Sciences Appliquées – 20 Avenue des Buttes de Coësmes, 35708 Rennes, France

ABSTRACT

The buckling behaviour of a steel member is greatly dependent on the residual stress distribution, which is affected by the fabrication process. Indeed, residual stresses in welded steel members are significantly influenced by possible flame-cuts at the flange tips commonly used in practice. However, the Eurocode 3 rules do not account for the beneficial effects of the flame-cuts. Experimental data on commonly used slender members are limited, and therefore to gain further insight an experimental test campaign involving eight slender welded members is carried out. The influence of the flange dimensions and fabrication process was investigated. A new residual stress model is proposed for welded I-sections made of flame-cut flanges integrating results from the literature. Moreover, the actual buckling behaviour of welded members made of flame-cut flanges and/or with a cross section that is not uniform and doubly symmetric is studied. A literature overview of past experimental works highlights the lack of results on common mono-symmetric and/or tapered members, especially for welded members made of flame-cut flanges. An experimental study was thus conducted including lateral-torsional buckling tests on four beams: two uniforms and two tapered. Both types of beams comprised a doubly symmetric and a mono-symmetric I-section. The benefits resulting from tapering and/or increasing the compression flange thickness of an I-section beam are highlighted. The experimental results validate the use of a finite element model for studying the impact of the flange fabrication process on the lateral-

torsional buckling resistance. Flame-cuts present at both flange ends increase the ultimate resistance.

Keywords: Residual stresses, Welded I-section, Flame-cut flanges, Lateral-torsional buckling.

1 INTRODUCTION

Buckling of steel members is strongly affected by geometrical and material imperfections. The existing design rules of Eurocode 3 Part 1-1 [1] are therefore based on experimental and numerical results from studies conducted on various types of steel members. Concerning welded members, the code rules are based on the assumption of hot-rolled flanges. However, other fabrication techniques that result in various residual stress distributions exist in practice ([2]-[4]). In particular, wide hot-rolled plates divided into several flanges using longitudinal flame-cuts are commonly used. These thermal torch cuts induce very localized high temperatures at the free ends of the plate, producing tensile residual stresses as the plate cools unevenly [2]. However, few experimental measurements of residual stresses in flame-cut flanges can be found in the literature. Existing models for residual stresses of I-sections with flame-cut flanges have been proposed [2], [5]-[12] with clearly different values of stress magnitude. In particular, there is strong disagreement regarding the compressive stresses on the flanges and the tensile stresses at the flange tips. Although relying on extensive experimental work, two recent studies by Schaper et al. [5] and Unsworth et al. [11] yielded contrasting models. The latter suggests a stress at the flange tips equal to zero while the former recommends approximately 40% of the yield strength for a S355 steel. Besides, the dimensions of the specimens tested were quite different. Residual stress tests were performed on stocky cross-sections ([3]-[5], [8], [10]-[12]), whereas in practice welded members are generally slender. Experimental data are thus needed for common slender cross-sections.

Large-scale tests were run in the past to investigate the effect of flame-cuts made at the flange tips on the out-of-plane buckling of steel members. Tests were also used to cope with the lack of consistency of Eurocode 3 Part 1-1 [1] single method for non-uniform members (see [13] to [15]).

Prawel et al. [16] presented an experimental study including three tests on tapered welded beams subjected to a linear bending moment and resting on fork supports. Furthermore, 12 tapered or uniform cantilever beam-columns were also tested. The latter were made of either flame-cut or hot-rolled flanges while the beams had hot-rolled flanges. Residual stresses were measured in both types of flanges. No mono-symmetric member was studied and the thickness of the flanges and web were only 6.35 and 2.67 mm, respectively, which is far from the values found in common practice. Consequently, the failure modes featured local buckling of the flanges. However, the higher resistance of welded members with flame-cut flanges when compared to similar specimens with hot-rolled flanges was highlighted.

As part of the ESCS Steel RTD Programme [17], lateral-torsional buckling tests were performed on four doubly symmetric tapered specimens. The welded specimens were made of hot-rolled flanges and subjected to a linear bending moment distribution. More recently, Tankova [18] presented experimental investigations on six S355 doubly symmetric welded cross-sections made of flame-cut flanges loaded in bending, compression or combined bending and compression. The residual stresses of compressed members were measured. This study was used as the experimental background for a new design method to assess the stability of a steel member with, or without, a doubly symmetric and uniform cross-section.

Schaper et al. [19] described experimental lateral-torsional buckling tests on eight uniform welded I-sections made of flame-cut flanges. Seven beams had a doubly symmetric cross-section and one beam had a mono-symmetric cross-section. The specimens were stocky with depth-to-width ratios of 1.13 to 2.15, although more slender beams are used in practice. Test results were used as the experimental bases for the modified method of the equivalent compression flange introduced in the revised Eurocode 3 Part 1-1 [20]. An original experimental study was also introduced by Ji et al.[21]-[22], focusing on the buckling behaviour of seven beams subjected to a distributed transverse load. All of the specimens were uniform with a doubly symmetric cross-section and made of either flame or plasma-cut flanges but they had thick plates (13 mm for the web and 25 or 32 mm for the flanges) and wide flanges (300–470 mm). These cross-sections are not commonly used in practice. Measurements of residual stresses performed on four of the

specimens were presented by Unsworth et al. [23]. The experimental ultimate loads in analogous specimens made of plasma or flame-cut flanges were quite close.

A scarcity of experimental studies investigating the out-of-plane buckling behaviour of welded members made of flame-cut flanges is noticed. Schaper et al. [19] and Ji et al. [21]-[22] investigated only uniform beams among which a single specimen had a mono-symmetric cross-section. Besides, the specimen dimensions corresponded to stocky I-sections, whereas slender cross-sections are commonly used in practice. Other experimental studies [16]-[18] investigated tapered members, but all specimens had a doubly symmetric cross-section. Experimental tests are thus needed that cover geometries used in practice and particularly slender cross-sections, mono-symmetric members as well as tapered beams.

The objective of this paper is thus to study the stability of welded I-section members commonly used in practice and in particular to highlight the impact of residual stresses. First, the paper focuses on the distribution of residual stresses in welded I-section members. A literature overview concerning existing models adapted to hot-rolled or flame-cut flanges is presented. Owing to differences between existing models, an original experimental study is described. This study investigates the residual stress distribution in eight S355 welded members for which the flange fabrication process and dimensions vary. A residual stress model is proposed for welded members made of flame-cut flanges based on existing measurements as well as on experimental test results presented in this paper. The stress distribution depends on the flange slenderness and on the cross-section depth-to-width ratio.

To compensate for the lack of experimental results, a new experimental study is presented in Section 3. This study consists in lateral-torsional buckling tests performed on four S355 slender I-section beams. Two uniform and two tapered beams were tested with a doubly symmetric and a mono-symmetric cross-section for both types of beams.

Finally, the specimens tested are modelled with ANSYS including the measured geometrical imperfections and residual stresses. Numerical and experimental results are in good agreement. The specimens are also modelled taking into account the residual stress patterns for flame-cut or

hot-rolled flanges, but also disregarding residual stresses. An average of 10% deviation is obtained between the ultimate loads using both residual stress models. Further analyses are performed on the uniform doubly symmetric test specimen under a constant bending moment with varying slenderness. Using the residual stress model adapted to flame-cut flanges yields ultimate bending moments up to 15% greater than when using the residual stress model for welded beams made of hot-rolled flanges. These results advocate the use of distinct design methods that depend on the flange fabrication process.

2 RESIDUAL STRESSES IN WELDED I-SECTION MEMBERS

2.1 Existing models

2.1.1 Welded members with hot-rolled flanges

While the current Annex C of Eurocode 3 Part 1-5 [24] does not recommend any residual stress model for welded members, a model is provided in prEN 1993-1-14 [25]. This stress pattern is based on the model proposed by ECCS [26] corresponding to welded members made of hot-rolled flanges (see Figure 1). The tensile stresses at the flange-to-web junctions reach the yield strength f_y. These are compensated by compressive stresses reaching a quarter of f_y in the remaining parts.

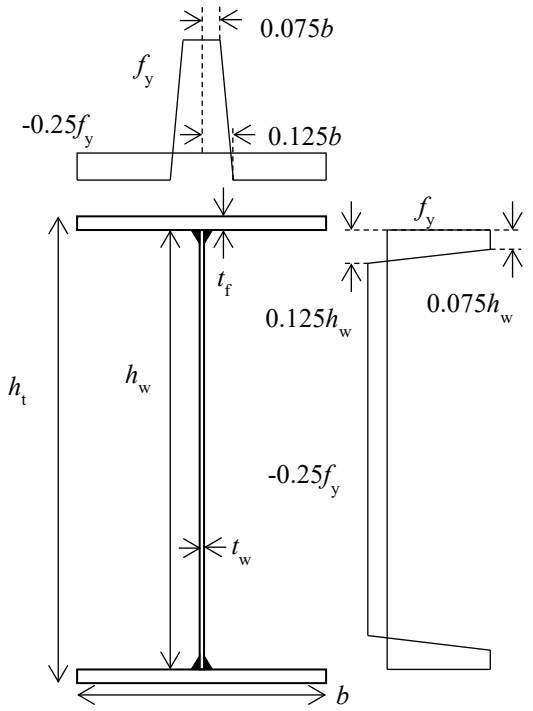

Figure 1: Residual stress model of prEN 1993-1-14 [25] (hot-rolled flanges)

The Swedish standard BSK 99 [27] proposes an analogous model (see Figure 2a)) but the widths of the stress blocks are defined using the web and flange thicknesses, i.e. t_w and t_f, respectively. The compressive stress is determined from self-equilibrium. Gozzi [28] used an adaptation of the BSK 99 [27] model (see Figure 2b)) in which stresses are uniform in tension and compression.

For mono-symmetric members, Trahair [29] suggests a model with different compressive stresses in both flanges, with the tensile stresses reaching the yield strength (see Figure 2c)). One may

note the absence of residual stresses in the web, justified by the negligible influence of web yielding on out-of-plane buckling.

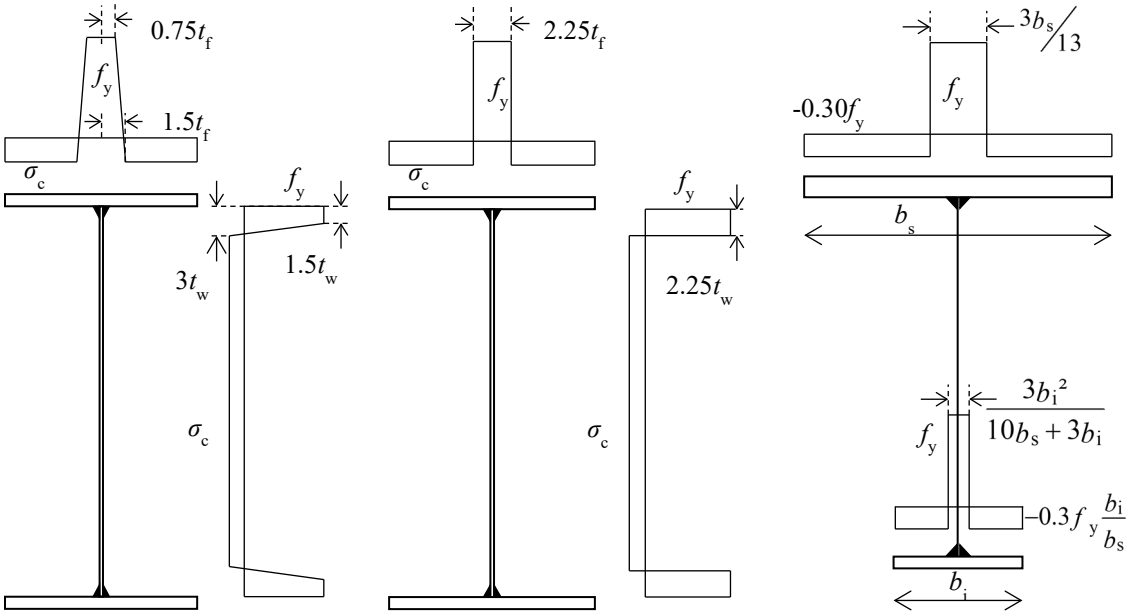

a) BSK 99 [27] b) Gozzi [28] c) Trahair [29]

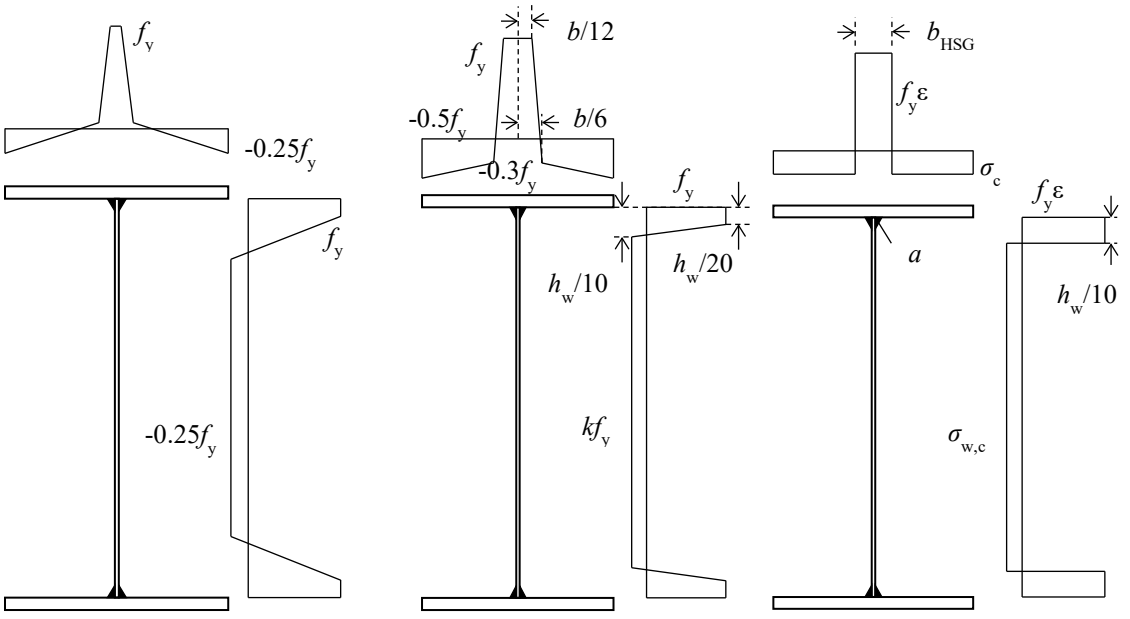

d) Kabir et al. [30] e) Prawel et al. [16] f) Schaper et al. [5]

Figure 2: Residual stress models for welded members made of hot-rolled flanges

Kabir et al. [30] proposed the residual stress pattern depicted in Figure 2d) featuring linear variations of the stress intensities. Again, tensile stresses at the flange-to-web junctions reach the yield strength. The peak compressive stress is similar to that of the prEN 1993-1-14 [25] model, i.e. -0.25f_y. Prawel et al. [16] proposed a similar shape (see Figure 2e)) resulting from

experimental measurements performed on tapered members. The tensile zone at the flanges centre is wider than in the previous models, and is almost $b/3$. The important tensile stresses are compensated by high magnitudes of the compressive stresses, which are up to half of the yield strength. Since the compressive stresses of the model by Prawel et al. [16] are very high, Kim [31] proposed to employ a modified "*best-fit Prawel*" model where the stress magnitudes in the flanges are reduced. The stress distribution remains unchanged in the web and a value of -0.176 is specified for parameter k. Liu [32] performed residual stress measurements using the hole drilling technique in S690 welded members. The tests results were used to validate a numerical model predicting residual stresses in welded members without thermal cuts at the flange tips. A parametric study was conducted that included S355 welded specimens. A clear effect of the thickness of the plates on the residual stress distribution was highlighted: the magnitude of the compressive stress in the flange decreases as the flange slenderness increases.

Schaper et al. [5] used existing and new experimental data to propose the model depicted in Figure 2f) for welded members made of hot-rolled flanges. Steel grades of S235 to S890 were investigated, with the flanges being either hot-rolled or flame-cut. The proposed model for welded members made of hot-rolled flanges exhibits tensile stresses at the flange-to-web junctions that do not attain the yield strength for steel grades greater than S235. Indeed, this model features stress magnitudes that are non-linearly dependent on f_y owing to the introduction of the parameter ε given by:

$$\varepsilon = \sqrt{235 / f_y} \tag{1}$$

Residual stress models for welded members made of hot-rolled flanges present an important tensile zone at the flange-to-web junctions compensated by compressive stresses in the rest of the cross-section. The tensile stresses reach f_y in every model except in that of Schaper et al. [5] that relies on the most important experimental background. Compressive stresses are generally up to 25–30% of f_y.

2.1.2 Welded members with flame-cut flanges

Schaper et al. [5] also proposed a residual stress model for welded members made of flame-cut flanges (see Figure 3a) and Table 1) based on tests performed using the sectioning method on 15 members from Bochum and 13 from Coimbra. The Bochum specimens had 200–350-mm wide flanges with a thickness of 12–40 mm and were made of S355 to S460 steel. All specimens had a 370-mm high web except for one with an 800-mm high web. The Coimbra team measured residual stresses in members made of S460 or S690 steel. The only two S460 specimens were stocky with web heights of 278 and 468 mm and with 300- or 200-mm wide flanges.

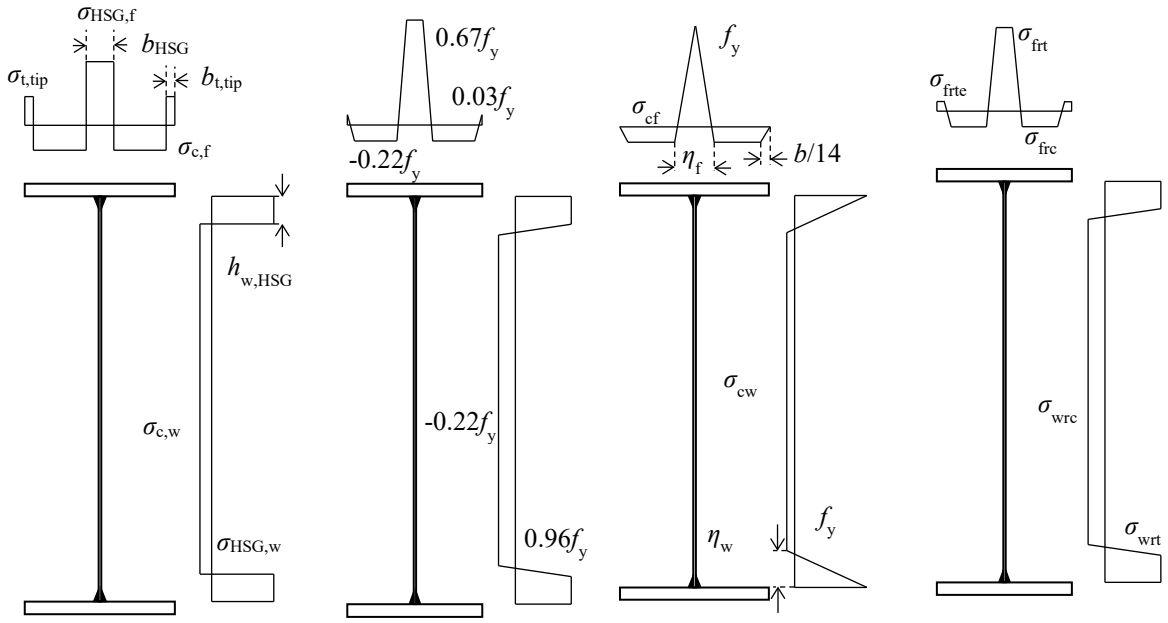

a) Models of Table 1 b) Yang et al. [10] c) Unsworth et al. [11] d) Ban et al. [12]

Figure 3: Residual stress models for welded members made of flame-cut flanges

When comparing both models proposed by Schaper et al. [5] for welded members made of hot-rolled (see Figure 2f)) and flame-cut flanges (see Figure 3a)), the major influence of the flange fabrication process is seen at the flange tips. Indeed, the tips of hot-rolled flanges contain the peak value of the compressive stresses while flame-cut flanges exhibit tensile stresses. According to the model of Schaper et al. [5] for members with flame-cut flanges, the tensile stresses at the tips attain values of $0.41f_y$ and $0.36f_y$ in S355 and S460 steel members, respectively. Besides, the width and stress intensity of the tensile region at the flange centre is similar in both of the Schaper et al. [5] models.

The model proposed by ECCS [2] is depicted in Figure 3a) with the values of stresses and widths listed in Table 1. All the tensile stresses reach the yield strength. Expressions are provided to compute the widths c_i but they result in very thin tensile stress blocks at the flanges tips. Barth et al. [6] and Chacón et al. [7] proposed modified versions of the ECCS [2] model presented in Figure 3a) with the values from Table 1. The tensile stresses reach 33% and 18% of f_y at the flange centre and tips, respectively. One may note that the model of Chacón et al. [7] is not self-equilibrated owing to a wide tensile zone at the flange centre.

A residual stress shape is suggested by Wang et al. [8] based on experimental data obtained using the sectioning and the hole-drilling methods on three S460 members. The shape corresponds to that in Figure 3a) with different magnitudes given in Table 1 for the three members tested. The depth of the cross-sections varied between 168 and 320 mm while their width ranged between 156 and 314 mm. Both measurement techniques resulted in similar average values of compressive stresses, although the hole-drilling method provided more scattered results. Different magnitudes of residual stresses were measured in the three specimens. Values ranging between 8% and 48% of the yield strength were measured at the flange tips, with their compressive stresses varying between -0.20f_y and -0.41f_y.

Model	Flanges					Web		
	$b_{t,tip}$	b_{HSG}	$\sigma_{t,tip}/f_y$	$\sigma_{c,f}/f_y$	$\sigma_{HSG,f}/f_y$	$h_{w,HSG}$	$\sigma_{c,w}/f_y$	$\sigma_{HSG,w}/f_y$
ECCS [2]	c_f	$2c_2$	1	/	1	c_{fw}	/	1
Schaper et al. [5]	$b/16$	$\min\left\{\begin{matrix} t_w+5a \\ b/5 \end{matrix}\right\}$	0.5ε	/	ε	$h_w/10$	/	ε
Barth et al. [6]	$b/10$	$b/5$	0.18	-0.17	0.33	$h_w/20$	-0.07	0.63
Chacón et al. [7]	$b/20$	$9b/20$	0.18	-0.20	0.33	$h_w/10$	-0.15	0.63
Wang et al. [8]	$b/20$	/	0.08 to 0.49	-0.50 to -0.41	0.73 to 1.04	/	-0.15 to -0.24	0.73 to 1.04
Thiébaud [9]	$b/20$	$b/10$	0.20	-0.11	0.68	$h_w/20$	-0.07	0.63

Table 1: Parameters of the residual stress models

Using the sectioning method, Thiébaud [9] measured the residual stresses in flame-cut flanges of bridge girders before and after web welding. The S355 flanges studied were 60-mm thick and

their width ranged between 615 and 730 mm. The impact of the central weld on the flange compressive stresses was highlighted, while the tip stresses remained unchanged before and after welding. This study yielded the model shown in Figure 3a) with the values presented in Table 1. A low magnitude of compressive stresses in the flanges is observed, which is 11% of the yield strength. The tensile blocks at the flange tips are similar to those of the model by Chacón et al. [7] model with a magnitude of $0.20f_y$ and a width of $b/20$.

Yang et al. [10] also measured residual stress distributions with the sectioning method in four members. The specimens had a nominal yield strength of approximately 345 MPa with depths of 300–400 mm. The flanges of three of the members were 10-mm thick and 200-mm wide. The last one was mono-symmetric with flanges widths of 180 and 220 mm. The experimental results were used to propose the model depicted in Figure 3b) where only the peak stresses are provided. The tensile stresses at the flange tips attain only 3% of the yield strength, which is very low when compared to the previous models where values of 18–100% of f_y are recommended.

The sectioning method was also employed by Unsworth et al. [23] to measure the stress distributions in four welded members: one with flame-cut flanges and three with plasma-cut flanges. The test specimens had a nominal yield strength of 350 MPa. The overall depth and width ranged between 536 and 759 mm, and between 300 and 430 mm, respectively. The flanges were 25.4 to 31.8-mm thick. Unsworth et al. [11] used original experimental measurements along with data of 25 specimens from the literature to propose the model presented in Figure 3c). The analysed data concerned mostly stocky members with a web height of up to 430 mm and thickness greater than or equal to 8 mm, while the measured yield strength was between 362 and 799 MPa. This model is adapted to welded members having either flame- or plasma-cut flanges and with zero stress at the flange tips.

The experimental work of Ban et al. [12] focusing on S460 welded I-section members with flame-cut flanges should also be mentioned. Again, the sectioning method was employed to measure the residual stresses of eight compact members. Indeed, the depth and width ranged between 110 and 360 mm, and between 130 and 348 mm, respectively. The plate thickness were 10, 12 and 14 mm

with measured yield strength of 492 to 532 MPa. A model was proposed for S460 I-section members with flame-cut flanges based on the experimental results (see Figure 3d)).

2.1.3 Summary

Various patterns were proposed for the residual stresses of welded members made of flame-cut flanges. In the ECCS [2] model, tensile stresses reach f_y, resulting in very narrow stress blocks at the flange tips. In other models ([5]-[11]), the tensile stresses at the flange tips vary from 0 to $0.5f_y$. The magnitude of the compressive stresses range between 11% and 22% of the yield strength when explicitly provided.

The models of Wang et al. [8], Thiébaud [9] and Yang et al. [10] are based on few experimental results while those of Schaper et al. [5] and Unsworth et al. [11] rely on extensive experimental measurements. These data, which include high strength steel, concern mostly small and stocky cross-sections with a vast majority of Class 1 webs in pure bending according to EN 1993-1-1 [1]. A lack of data on members with a depth greater than 500 mm is noticed while in practice the depth of welded members is generally between 500 and 1200 mm in steel buildings. Experimental results are needed for members that have typical dimensions and steel grade.

A new experimental test campaign is therefore described next. This study included residual stress measurements in eight S355 welded members: six with flame-cut flanges and two with hot-rolled flanges. These experimental results will be analysed along with results from the literature, yielding a new residual stress model adapted to welded members made of flame-cut flanges.

2.2 Experimental study

2.2.1 Description

The experimental study consists in residual stress measurements performed on eight S355 specimens at Liège University. All specimens are 3 m long and have a 780×8-mm web i.e. Class 3 webs in pure bending according to EN 1993-1-1 [1], as welded beams are generally designed. Since the influence of the flange fabrication process and the flange dimensions are the focus of the study, the thickness of the flanges was set at 12, 15 or 20 mm and the width was 200 or 250 mm. The specimens were fabricated by welding first one side of the web with both flanges. They

were then turned over to weld the other side of the web to both flanges. The dimensions were chosen to represent common practice, the nominal values are given in Table 2. The specimens are labelled as follows:

- The 3 first letters refer to the fabrication process:
  - "Wfc" for **W**elded members with **f**lame-**c**ut flanges,
  - "Whr" for **W**elded members with **h**ot-**r**olled flanges,
- The central number corresponds to the width of the flanges (in mm),
- The final number is the thickness of the flanges (in mm).

One specimen had a mono-symmetric cross-section made of same flange width but with different flanges thicknesses (15 mm and 20 mm).

The actual material properties were also measured using three coupons for each thickness, i.e. 8, 12, 15 and 20 mm. The coupons were extracted from specimens *Wfc_250-12* for the 8- and 12-mm thick plates and *Wfc_200-15/20* for the 15- and 20-mm thick plates. The mean values of the measured modulus of elasticity E, yield strength f_y and ultimate tensile strength f_u are given in Table 3.

The residual stresses were measured at mid-span of the test specimens using the sectioning method. Longitudinal strips of 100 mm were initially depicted in a 200-mm long central zone and their lengths L_i were measured using an extensometer with ball bearings. The central zone was sawed transversally followed by longitudinal sawing of the strips initially laid out. Each sawing procedure was performed using a band saw cooled by oil and water to avoid any modification of the residual stresses. The final lengths L_f of the strips were then measured. The strip widths varied between 10 and 33 mm in the flanges, and between 34 and 78 mm in the webs.

Specimen	h_w (mm)	t_w (mm)	b (mm)	t_f (mm)	L (m)	Steel grade	Flange type
Wfc_200-15	780	8	200	15	3	S355	Flame-Cut (FC)
Wfc_200-15/20	780	8	200	15; 20	3	S355	FC
Wfc_250-15	780	8	250	15	3	S355	FC
Wfc_250-12	780	8	250	12	3	S355	FC
Wfc_200-20	780	8	200	20	3	S355	FC
Wfc_200-12	780	8	200	12	3	S355	FC
Whr_200-15	780	8	200	15	3	S355	Hot-Rolled (HR)
Whr_200-20	780	8	200	20	3	S355	HR

Table 2: Nominal properties of specimens for residual stress measurements

The initial and final lengths were used to determine the released uniaxial strains ε_x of both faces of each strip, except at the flange centre. Using Hooke's law, the corresponding stresses σ_x are obtained:

$$\varepsilon_x = \frac{L_i - L_f}{L_i} \quad (2)$$

$$\sigma_x = E\varepsilon_x \quad (3)$$

The resulting stress of a strip is the average between the values measured on both faces. The value measured on the outer surface of a flange centre is averaged with that measured in the closest strip of the web.

Thickness (mm)	E (N/mm²)	f_y (N/mm²)	f_u (N/mm²)
8	201501	427	552
12	203732	410	545
15	211527	417	549
20	205627	395	541

Table 3: Material properties of the residual stress specimens

2.2.2 Experimental stress distributions

The influence of the flange fabrication process on the residual stresses distribution is studied by comparing the results obtained with the two specimen pairs having similar dimensions but different flange types. Figure 4a) presents the residual stresses measured in the flanges of

specimens *Wfc_200-15* and *Whr_200-15*. Those measured in *Wfc_200-20* and *Whr_200-20* are presented in Figure 4b). The web stress distributions are depicted in Figure 5.

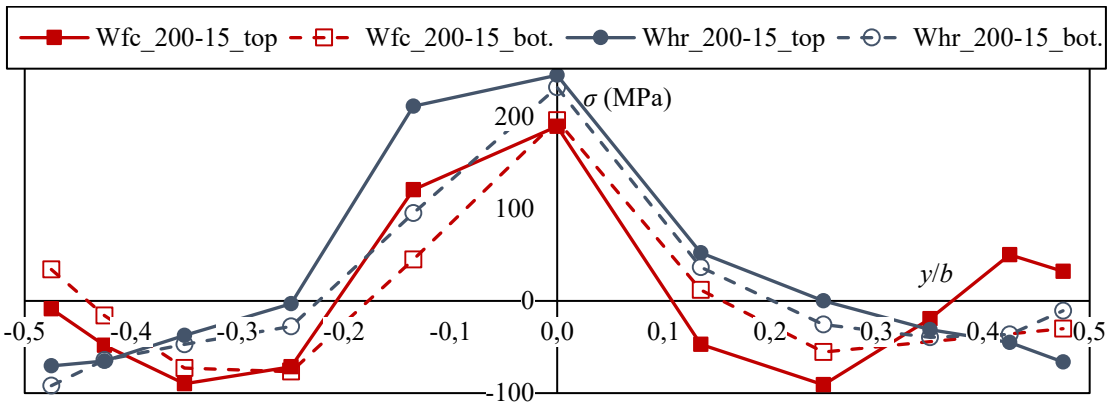

a) Residual stresses in 200×15-mm flanges

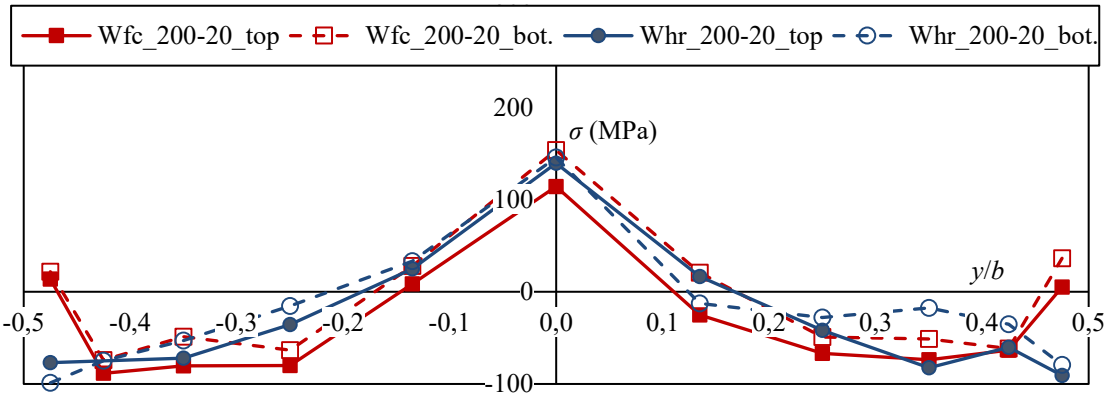

b) Residual stresses in 200×20-mm flanges

Figure 4: Residual stresses in hot-rolled and flame-cut flanges

Figure 4 shows substantial differences between hot-rolled and flame-cut flanges. Differences are clear at the tips where flame-cut flanges present low tensile stresses while hot-rolled flanges exhibit peak compressive stresses. These deviations are attributed to the flame-cutting process which induces high temperatures at the flanges ends. These thermal cuts thus provoke an uneven cooling of the plate which results in tensile stresses at its ends that are balanced by compressive stresses in the remaining part of the plate. The maximum compressive stresses are similar in the 15-mm thick flanges but are reached at different locations along the flange widths. This peak is obtained at the tips of the hot-rolled flanges and closer to the centre of flame-cut flanges. A similar conclusion can be drawn for the peak compressive stresses in the 20-mm thick flanges. Besides, the width of the central tension zone is greater in hot-rolled than in flame-cut flanges. The

magnitude of compressive stresses is lower in the webs of specimens with hot-rolled than in those with flame-cut flanges while greater tensile stresses are found.

Figure 4 and Figure 5 highlight the clear influence of the flange fabrication process on the residual stress distribution, proving relevant the use of distinct models for welded members made of hot-rolled or flame-cut flanges.

Among welded members made of flame-cut flanges, the influence of the flange dimensions on the stress distribution is investigated. To that end, members with flanges of 200- or 250-mm width but with the same thickness are compared. The residual stress distributions measured in specimens with 12 mm and 15 mm flange thickness are presented in Figure 6a) and Figure 6b), respectively. A decrease in the peak compressive stress as the flange width increases is observed owing to the larger space available to compensate the tensile stresses resulting from the welding process and flame-cuts. No influence of the flange width on the tip stress is observed in specimens with 15-mm thick flanges. However, a slight decrease of the magnitude of the tensile stresses is observed at the tip of specimens with 12 mm flanges. The deviation is mainly visible at the bottom flange of specimen *Wfc-200-12* and might be attributed to uneven initial residual stresses within the plate, prior to flame-cutting and welding. The width of the central tension zone is similar in 12-mm thick flanges but it increases as the width decreases in the 15-mm flanges.

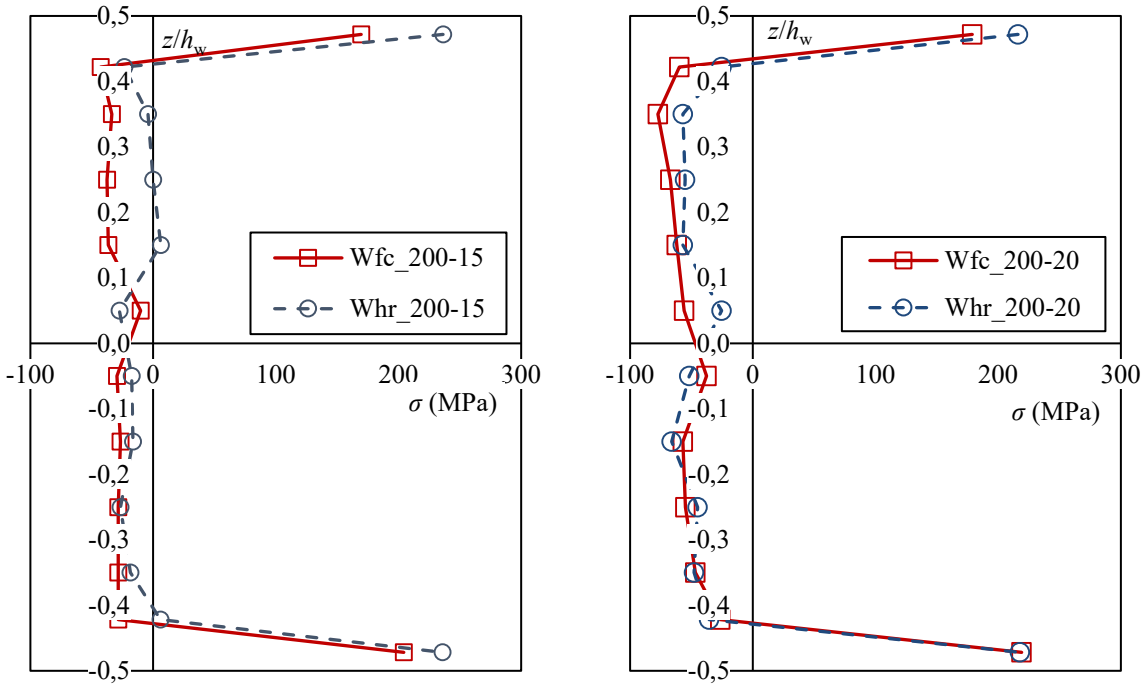

a) Specimens with 15-mm thick flanges b) Specimens with 20-mm thick flanges

322 **Figure 5: Residual stress in the webs of specimens with hot-rolled or flame-cut flanges**

323 The stress distributions in the web of specimens with two 12- or 15-mm thick flame-cut flanges
324 are presented in Figure 7a). No clear effect of the flange width on the stress distribution is
325 observed.

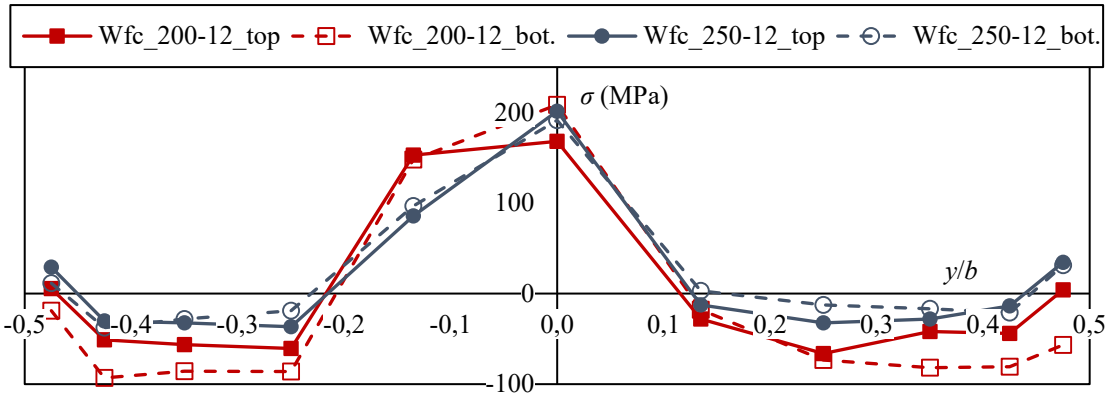

326
327 a) Residual stresses in 12-mm flame-cut flanges

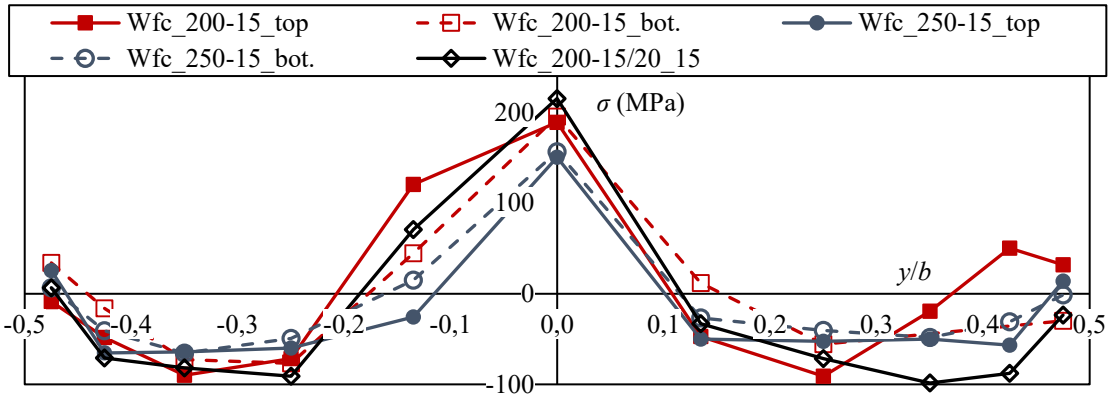

b) Residual stresses in 15-mm flame-cut flanges

Figure 6: Residual stresses in flame-cut flanges with varying width

The residual stress distributions are presented in Figure 7b) for both the doubly symmetric specimens (*Wfc_200-15*, *Wfc_200-20*) and for the mono-symmetric specimen (*Wfc_200-15/20*). An impact of the mono-symmetric design is noted in the web compressive stresses, with tensile stresses being similar in both doubly symmetric members. Indeed, a lower peak compressive stress is observed in the specimen with 15-mm thick flanges in comparison with the 20-mm thick flanges specimen while a somewhat higher magnitude is noticed in the 15 mm flanges in comparison with peaks in 20 mm ones. One may assume that most part of the balancing compressive stresses in the specimen with 20-mm thick flanges are found in its web owing to the important ratio between the plates thicknesses (t_f/t_w = 2.5). The mono-symmetric member has lower compressive stresses near the 15 mm top flange than near the 20 mm bottom flange.

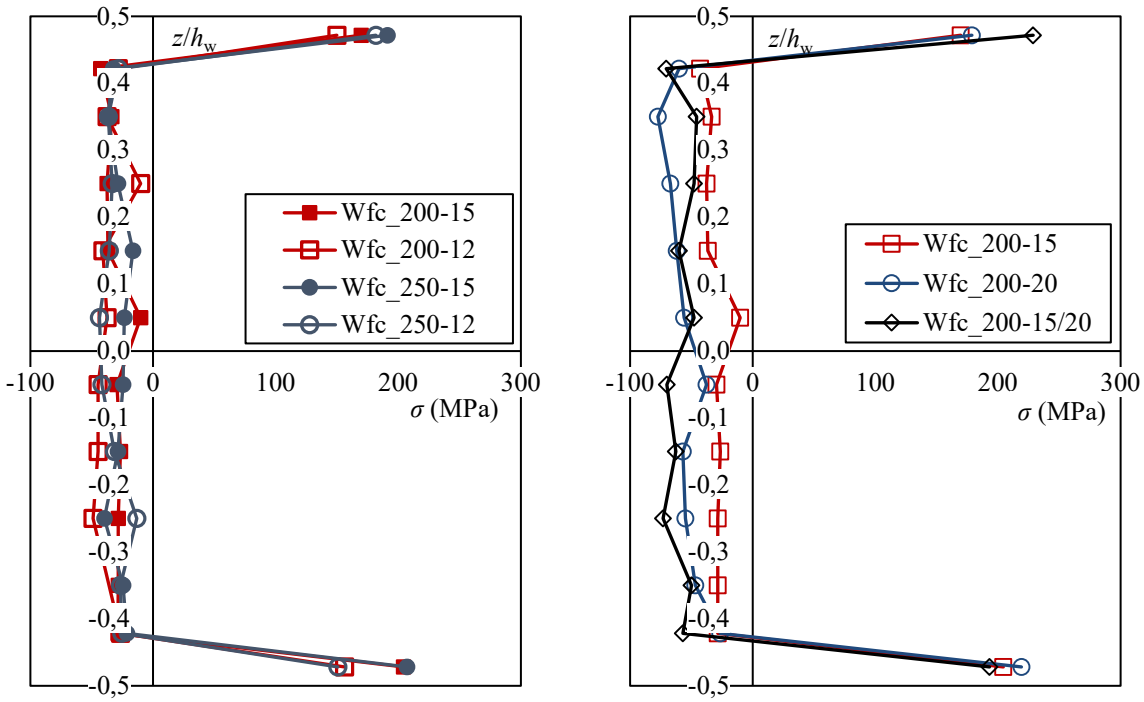

a) Specimens with 12- or 15-mm thick flanges

b)Specimens with 200×15- or 20-mm flanges

341 **Figure 7: Residual stresses in the webs of specimens with flame-cut flanges**

342 Experimental distributions in 200×15-mm flame-cut flanges are presented in Figure 8 while those
343 in 200×20-mm flanges are shown in Figure 9. No major differences are observed between the
344 three 200×15-mm flame-cut flanges except near the right end (y>0) where discrepancies are
345 noted. There are also no significant differences between the three 200×20-mm flame-cut flanges.
346 The mono-symmetric design has no visible effect on the stress distribution in the flanges, with
347 only a small influence seen in the web.

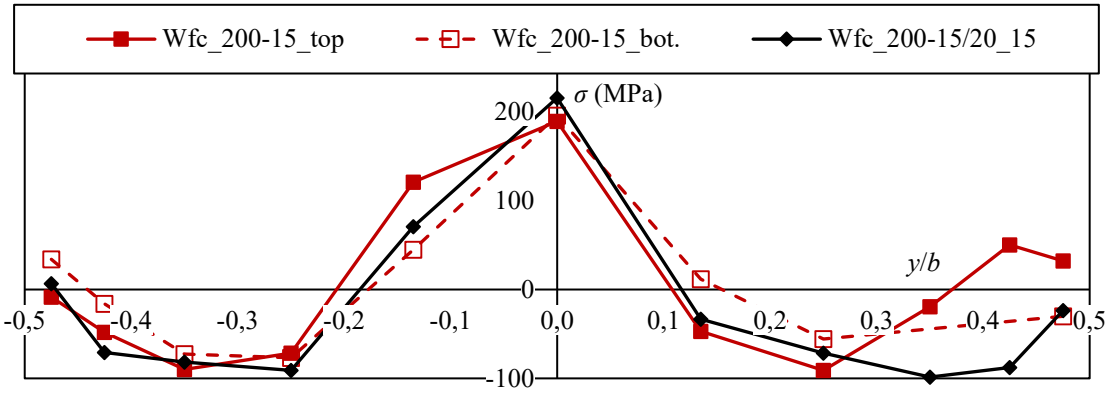

348

349 **Figure 8: Residual stresses in 200×15-mm flame-cut flanges**

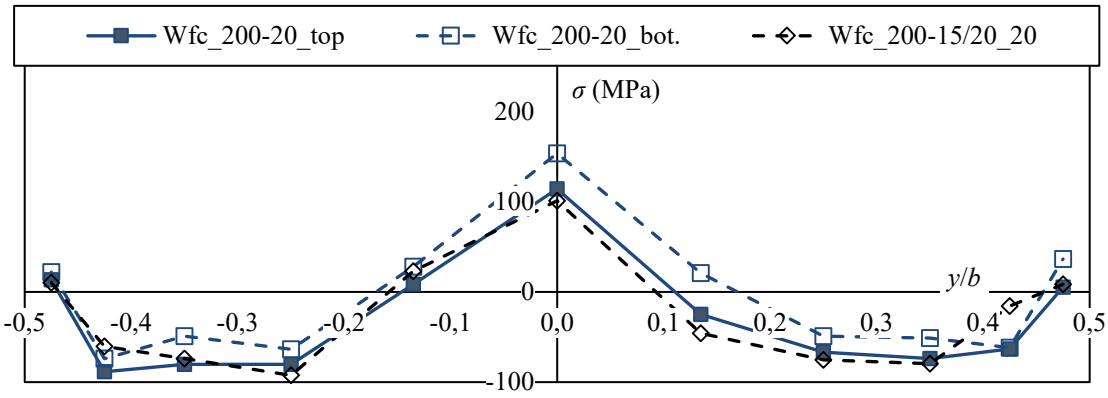

Figure 9: Residual stresses in 200×20-mm flame-cut flanges

The measured distributions do not match with existing models for welded members made of flame-cut flanges (see Figure 3 and Table 1). Indeed, the predicted tensile stresses at the flanges tips are significantly over-estimated by the models of ECCS [2], Schaper et al. [5], Barth et al. [6], Chacón et al. [7], Wang et al. [8] and Thiébaud [9]. Those of Yang et al. [10] and Unsworth et al. [11] are closer, suggesting $0.03f_y$ in tension and 0, respectively. The peak compressive stresses are closer to the predictions of the models by Barth et al. [6], Chacón et al. [7] and Yang et al. [10] that range between $-0.17f_y$ and $-0.22f_y$.

Since the comparison between experimental results and existing models showed discrepancies, these experimental data are analysed in the following sub-section along with data extracted from the literature.

2.3 Residual stress model for welded I-sections made of flame-cut flanges

A residual stress model dedicated to welded members made of flame-cut flanges is proposed based on the experimental measurements of the present study and existing tests from the literature presented in Table 4. These additional results are distributions measured in the past 10 years on welded I-sections made of flame-cut flanges with a yield strength of up to 460 MPa. Since the model is suited to steel building members, the data analysed from the literature concern members with web and flange thicknesses between 5 and 15 mm, and between 8 and 40 mm, respectively. The 20 specimens extracted from the literature are from studies which have yielded the models depicted in Figure 3a), Figure 3b) and Figure 3c). The nominal yield strengths of the specimens

372 are between 345 and 460 MPa. Additional data relate to mostly small and stocky H-sections, with
373 only two specimens having a web height greater than 400 mm. The flange widths are more in line
374 with common practice, ranging from 100 to 400 mm. The same applies to the web and flange
375 thickness, which are comprised between 6 and 12.7 mm, and between 8 and 40 mm, respectively.
376 The experimental residual stress distributions are characterized using parameters proposed by
377 Unsworth et al. [23]. The parametric compressive stress σ_{pc} and width η of the high stress gradient
378 (HSG) regions at the flange-to-web junctions are determined for the web and flanges of specimens
379 listed in Table 2 and Table 4. The parametric compressive stress can be understood as the mean
380 stress of the "uniformly" compressed part of a plate:

$$\sigma_{pc} = \frac{1}{n}\sum_{i=1}^{n}\sigma_{rc,i} = \overline{\sigma_{rc}} \tag{4}$$

381 where σ_{rc} represents the residual stresses in a plate that satisfy:

$$\sigma_{rc} = \sigma_{res} \forall \sigma_{res} \leq \overline{\sigma_{res}} - 0,25\sqrt{\frac{1}{n}\sum_{i=1}^{n}\left(\sigma_{res,i} - \overline{\sigma_{res}}\right)^2} \tag{5}$$

382 where σ_{res} are the residual stresses in the plate studied.

383

Reference	Specimen	h_w (mm)	t_w (mm)	b (mm)	t_f (mm)	$f_{y,w}$ (N/mm²)	$f_{y,f}$ (N/mm²)
Yang et al. [10]	H1	280	8	200	10	398	458
	H2	380	8	200	10	398	458
	H3	380	8	200	10	398	458
	H4	332	8	220(1) 180(2)	10(1) 8(2)	398	458(1) 398(2)
Tankova et al. [33]	RS_1	317	12	100	12	377	377
	RS_2	230	6	110	12	362	371
	RS_5	311	10	100	16	451	386
	RS_6	143	10	100	16	443	392
Schaper et al. [19]	Pos. 1	370	8	350	20	365	357
	Pos. 3-1	370	8	200	20	351	340
	Pos. 4-1	370	8	350	12	402	444
	Pos. 5	370	8	200(1) 350(2)	20(1) 40(2)	462	334
	Pos. 1*	370	8	350	20	363	357
	Pos. 3-1f$_y$	370	8	200	20	554	452
	Pos. 4-2	370	8	350	40	356	353
	Pos. 3-2	370	8	350	20	365	450
	Pos. 1f$_y$	370	8	350	20	552	444
Unsworth et al. [23]	SP2_2	600	12.7	430	31.8	364	347
Schaper et al. [5]	B1	468	8	200	16	Not specified (*S460*)	
	B4	278	8	300	16	Not specified (*S460*)	

Table 4: Geometrical and mechanical characteristics of specimens from the literature

Besides, the HSG area at the flanges centre is defined as the region between the two closer locations of the compressive stress $\sigma_{p\eta}$ given by:

$$\sigma_{p\eta} = \overline{\sigma_{res}} + 1{,}5\sqrt{\frac{1}{n}\sum_{i=1}^{n}\left(\sigma_{res,i} - \overline{\sigma_{res}}\right)^2} \quad (6)$$

The HSG widths are defined in the web from the flange junction to the location of $\sigma_{p\eta}$. Linear interpolations are used to evaluate the locations of the compressive stresses $\sigma_{p\eta}$.

Reference	Specimen	σ_{pc}/f_y		η/plate width		σ_{tip}/f_y
		Flanges	Web	Flanges	Web	
Authors (§2.2)	Wfc_200-15	-0.17	-0.08	0.37	0.08	0.02
	Wfc_200-12/20	-0.19	-0.14	0.41	0.07	0.00
	Wfc_250-15	-0.12	-0.06	0.34	0.08	0.03
	Wfc_250-12	-0.06	-0.08	0.41	0.08	0.06
	Wfc_200-20	-0.17	-0.14	0.46	0.10	0.05
	Wfc_200-12	-0.16	-0.09	0.42	0.08	-0.04
Yang et al. [10]	H1	-0.14	-0.25	0.33	0.15	0.06
	H2	-0.09	-0.20	0.36	0.10	-0.02
	H3	-0.12	-0.13	0.36	0.11	0.02
	H4	$-0.11^{(1)}$ $-0.20^{(2)}$	-0.18	$0.37^{(1)}$ $0.40^{(2)}$	0.13	$0.07^{(1)}$ $0.00^{(2)}$
Tankova et al. [33]	RS_1	-0.25	-0.43	0.55	0.15	0.08
	RS_2	-0.12	-0.12	0.29	0.22	-0.03
	RS_5	-0.15	-0.31	0.48	0.14	0.22
	RS_6	-0.31	-0.39	0.36	0.31	0.11
Schaper et al. [19]	Pos. 1	-0.21	-0.04	0.13	0.11	0.33
	Pos. 3-1	-0.26	-0.18	0.32	0.11	0.17
	Pos. 4-1	-0.14	-0.10	0.33	0.11	-0.09
	Pos. 5	$-0.25^{(1)}$ $-0.14^{(2)}$	-0.03	$0.27^{(1)}$ $0.28^{(2)}$	0.19	$0.08^{(1)}$ $0.12^{(2)}$
	Pos. 1*	-0.15	-0.09	0.18	0.11	0.36
	Pos. 3-1f_y	-0.22	-0.09	0.21	0.11	0.33
	Pos. 4-2	-0.14	Tensile stresses	0.24	0.32	0.35
	Pos. 3-2	-0.13	-0.06	0.14	0.11	0.41
	Pos. 1f_y	-0.13	-0.08	0.16	0.11	0.46
Unsworth et al. [23]	SP2_2	-0.14	-0.17	0.20	0.26	0.03
Schaper et al. [5]	B1	-0.20	-0.20	0.39	0.12	0.15
	B4	-0.15	-0.21	0.36	0.17	0.07

Table 5: Characteristic parameters of experimental residual stress distributions

The average parametric compressive stresses, the widths of the HSG regions and the mean stresses measured at the flange tips σ_{tip}. are presented in Table 5. The parametric compressive stresses in

393 the flanges are mostly between 12% and 17% of the yield strength, although some specimens
394 exhibit higher values, i.e. up to 31% of f_y. Compressive stresses are slightly lower in the webs,
395 with most of them ranging between 8% and 14% of the yield strength. The widths of the HSG
396 regions in the flanges and webs vary clearly. The widest zones correspond to the highest ratios of
397 the cross-section depth to the flange widths.

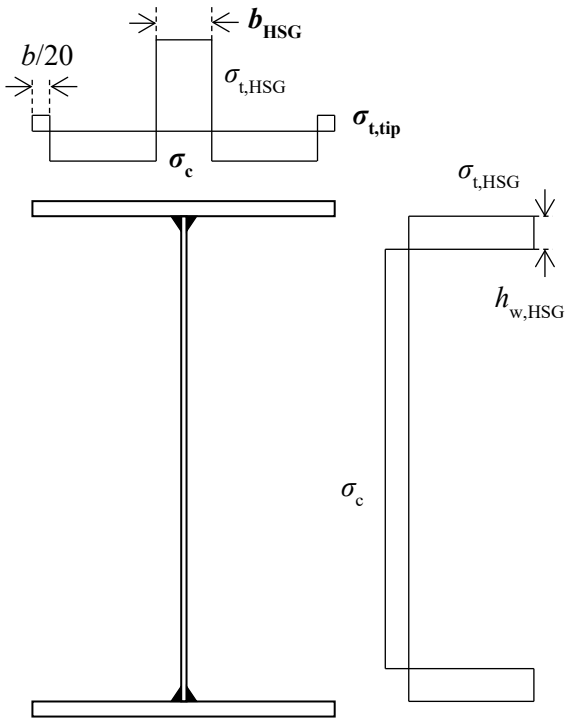

398

399 **Figure 10: New residual stress model for welded members with flame-cut flanges**

400 A new model, depicted in Figure 10, is proposed based on these experimental results. This new
401 model consists in stress blocks with constant stress intensities to ease incorporation of residual
402 stresses in Finite Element Analyses. Characterizing the residual stress model, σ_c, $\sigma_{t,tip}$ and b_{HSG}
403 should be computed first:

$$\sigma_c = -f_y\left(0.25 - 0.005\frac{b}{t_f}\right) \le -0.14 f_y \tag{7}$$

$$\sigma_{t,tip} = f_y\left(0.70 - 0.35\frac{h_t}{b}\right) \ge 0.03 f_y \tag{8}$$

$$b_{HSG} = 0.1b + 0.036h_t \tag{9}$$

The experimental results scatter (see Table 5) motivated the introduction of model parameters with varying values. Consequently, the experimental values of σ_c, $\sigma_{t,tip}$ and b_{HSG} were plotted with respect to various geometrical properties in turn. The best tendencies were observed when plotting σ_c against b/t_f and both $\sigma_{t,tip}$ and b_{HSG} against h_t/b.

The width b_c of the compressive stress blocks in the flanges and the tensile stress $\sigma_{t,HSG}$ at the flange centre are obtained from flange self-equilibrium. The new model can be applied to doubly symmetric or mono-symmetric members. The magnitude of the web compressive stresses is the average of the magnitudes in both flanges. The intensity of the web tensile stresses is the mean of the stresses in the HSG regions of both flanges. The stress block widths are determined from web self-equilibrium.

The compressive and tip stresses in the flanges computed using expressions (7) and (8) are presented in Figure 11 and Figure 12, respectively. The experimental values from Table 5 are added for comparison. Experimental results show a decrease in the magnitude of the compressive stress as the flange slenderness increases. This trend is well represented by the model predictions for which a limit value of $-0.14f_y$ is introduced. Expression (7) underestimates the magnitude of the compressive stress in some cases, especially for stocky flanges.

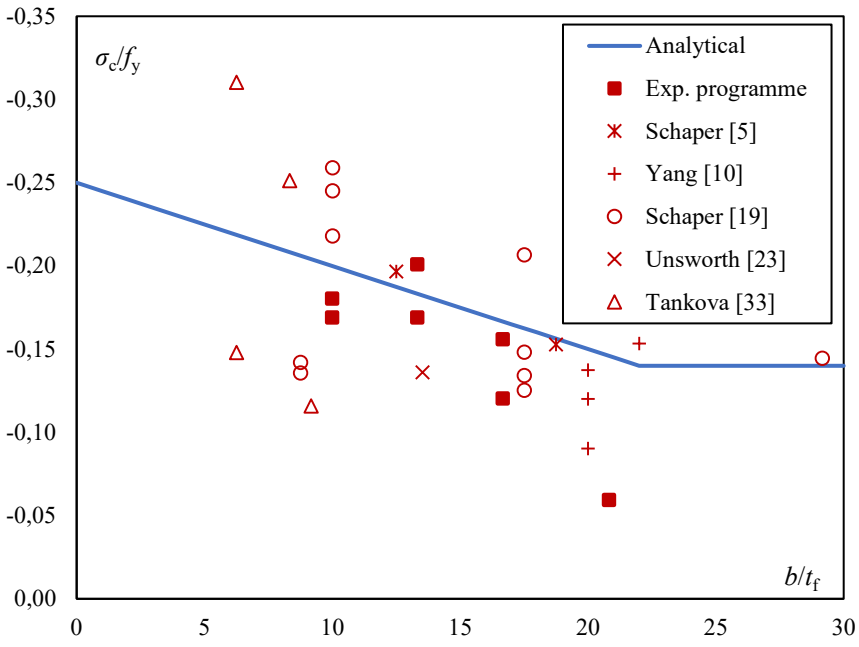

Figure 11: Flanges compressive stresses: Experimental and analytical results

Similarly, the experimental results plotted in Figure 12 highlight a decrease in the tip stress magnitude as the cross-section depth-to-width ratio increases. The predictions of expression (8) match well with most experimental results. For a few results, expression (8) slightly overestimates the magnitude of the tip tensile stress.

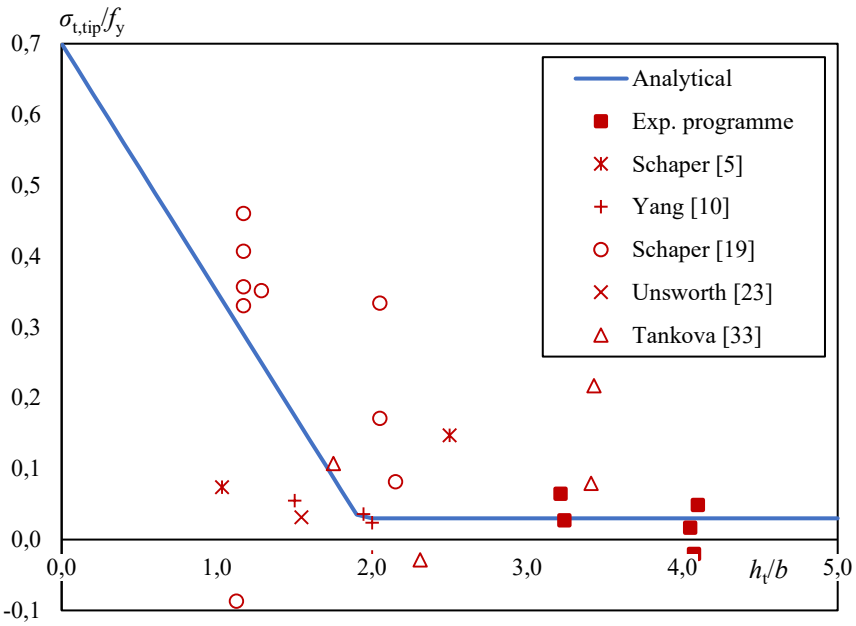

Figure 12: Flange tip stresses: Experimental and analytical results

Statistical parameters characterizing the deviation of the experimental results from the predictions of the new model are presented in Table 6 for the flange compressive and tip stresses. The mean deviations are very small, i.e. lower than 2.5% of f_y. Since the average differences are positive, the magnitude of the compressive stresses calculated analytically are greater than the experimental values. The analytical tip tensile stresses are lower than the measured values.

Parameter		
$\frac{\sigma_{c,exp} - \sigma_{c,Analytical}}{f_y}$	*M*	*1.4%*
	SD	4.54%
$\frac{\sigma_{t,tip,exp} - \sigma_{t,tip,Analytical}}{f_y}$	*M*	*2.4%*
	SD	15.81%

Table 6: Deviation between experimental and analytical results

The standard deviation for the compressive stress is very low, i.e. lower than $0.05f_y$. Results are more scattered regarding the flanges tip stresses, as depicted in Figure 12; the standard deviation is consequently more important, reaching 16% of the yield strength.

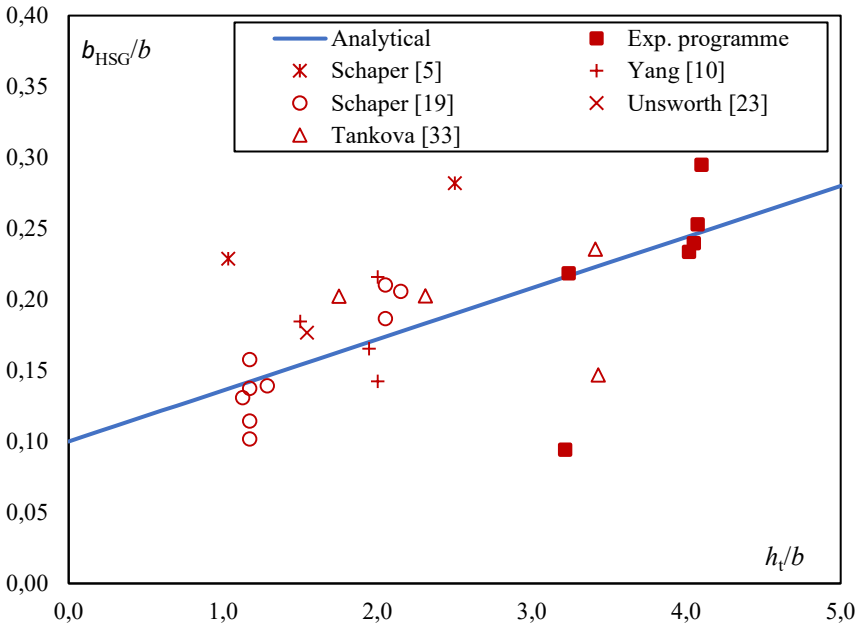

Figure 13: Width of the flange central tension region: Experimental and analytical results

Finally, the widths of the central HSG of the flanges region predicted by expression (9) are compared against experimental values in Figure 13. The experimental values show a clear increase in the HSG region width with the depth-to-width ratio, with expression (9) corresponding to an average increase.

Despite the scarcity of experimental distributions, especially for common slender members, a residual stress model is proposed. The model is dedicated to welded I-sections made of flame-cut flanges with a regular steel grade (i.e. up to S460). For direct use in non-linear finite element analyses, the model is defined by stress blocks that have constant intensities. The widths and magnitudes depend on the cross-section depth-to-width ratio and on the flange slenderness. The experimental data analysed include depth-to-width ratios of 1.03 to 4.10 and flanges slenderness ranging between 6.25 and 29.17, corresponding to the common practice of steel building members.

3 EXPERIMENTAL LATERAL-TORSIONAL BUCKLING OF WELDED BEAMS

3.1 Tests description

3.1.1 Full-scale specimens

An experimental study was conducted at Polytech' Clermont to better understand the lateral-torsional buckling of welded I-section beams made of flame-cut flanges. The tests were conducted on two uniform and two tapered beams. For both types of members, one has a doubly symmetric cross-section and the other a mono-symmetric cross-section. The specimens were composed of S355 steel. The beams, resting on fork supports at both ends, are loaded by a downward force applied at an intermediate cross-section (see Figure 14). The load jack is placed on the top flange of this cross-section restrained against lateral displacement and twist rotation and located at 2.18 m from the left support. The nominal dimensions of the members are presented in Figure 14 and Table 7. Both uniform beams have 786×8-mm Class 3 webs according to Eurocode 3 Part 1-1 [1]. In both tapered beams, the web height varies from 286 to 836 mm with a thickness of 8 mm. The flanges are 200-mm wide with a thickness of 15 mm, except for the compressive flanges of mono-symmetric beams that are 20-mm thick. Besides, transverse stiffeners are placed at each restrained cross-section. A longitudinal stiffener is welded along the 2.18 m-long part on both sides of the web to prevent web buckling. The specimen dimensions and steel grade are chosen in line with the current steel buildings practice.

Specimen	h_w (mm)	t_w (mm)	b (mm)	t_f (mm)	Steel grade	Total length (m)
U-DS	786	8	200	15	S355	8.83
U-MS	786	8	200	20*;15**	S355	8.83
T-DS	286 to 836	8	200	15	S355	8.83
T-MS	286 to 836	8	200	20*;15**	S355	8.83

Table 7: Nominal properties of tested specimens

*: Compression flange

**: Tension flange

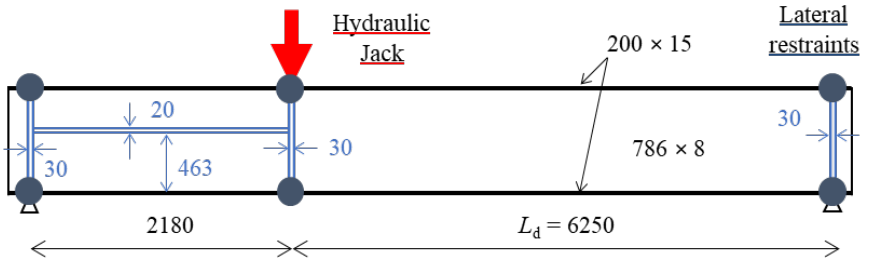

a) Specimen *U-DS*

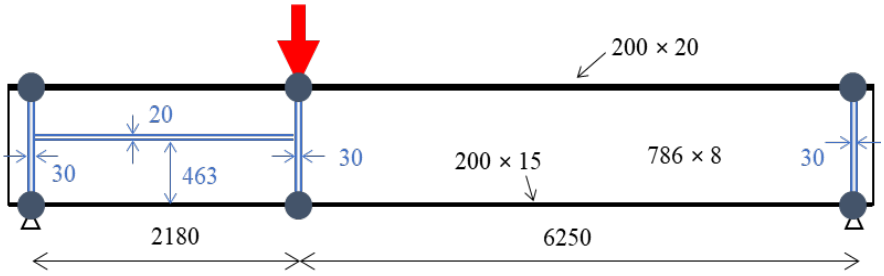

b) Specimen *U-MS*

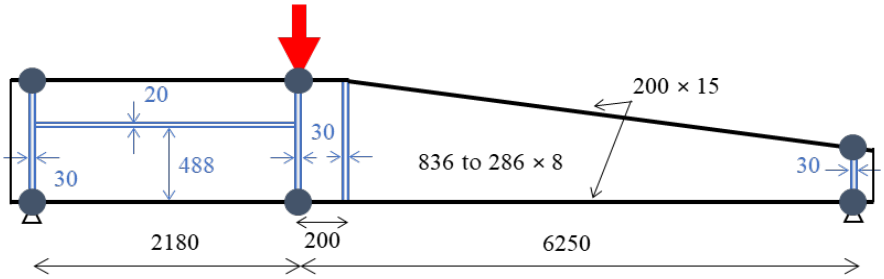

c) Specimen *T-DS*

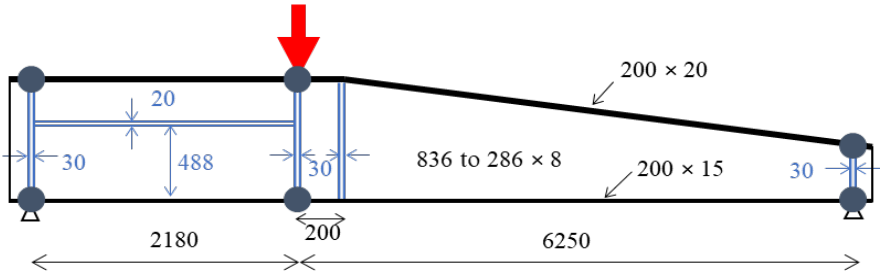

d) Specimen *T-MS*

Figure 14: Test specimens (dimensions in mm)

3.1.2 Material properties

The material properties have been measured on three coupons from 8- and 15-mm thick plates and four coupons from 20-mm thick plates. Apart from two 20-mm thick coupons extracted from the compression flange of *T-MS* (post-test), all coupons were extracted from additional plates of the same batch. The mean values of the measured Young modulus E, yield strength f_y and ultimate tensile strength f_u are given in Table 8.

Thickness (mm)	E (N/mm²)	f_y (N/mm²)	f_u (N/mm²)
8	203283	421	550
15	209049	411	542
20	197821	390	539

Table 8: Material properties of the specimens tested

3.1.3 Geometrical imperfections

The actual cross-section dimensions are measured on four transverse cross-sections located along the beam. The means of the actual values normalized to the nominal values are presented in Table 9. The mean deviation is 1% at most.

Dimension	*Mean*
Depth	1.000
Web height	0.999
Web thickness	1.005
Flange width	1.003
Flange thickness	1.011

Table 9: Measured dimensions of the specimens normalized to the nominal dimensions

Angles at the compression flange-to-web junctions were measured. Local geometrical imperfections in the web were also characterized at four transverse cross-sections along the members using a steel ruler connected to five callipers. The measured angles are given in Table 10 and the magnitudes of the local imperfections in Table 11. The latter are given in millimetres and normalized to the web height of the corresponding cross-section.

Specimen	U-DS	U-MS	T-DS	T-MS
Angle on the left side of the web	88.1°	87.8°	88.5°	88.7°
Angle on the right side of the web	90.3°	91.3°	90.4°	90.2°

Table 10: Angles at the compression flange-to-web junction

Table 10 demonstrates that the sum of the flanges angles is less than 180°, ranging between 178.4° and 178.9°, which characterizes local imperfections in the flanges attributed to welding.

Specimen	U-DS	U-MS	T-DS	T-MS
Amplitude of web local imperfections (mm)	1.3	3.7	2.1	1.6
Amplitude of web local imperfections as a function of h_w	h_w/584	h_w/214	h_w/293	h_w/485

Table 11: Amplitudes of web local imperfections

Table 11 shows a maximum value of the magnitude of web local imperfections of up to h_w/214, which is lower than the fabrication tolerance defined by EN 1090-2 [34] for 786×8-mm webs equal to h_w/163.

Furthermore, global geometrical imperfections were also measured. The measurements were performed on the compression flange with respect to a reference straight laser line. The magnitudes of the global imperfection are presented in Table 12 as absolute values and as a function of L_d. The results are all lower than L_d/1000, which is the fabrication tolerance defined by EN 1090-2 [34]. The magnitudes range between L_d/1911 and L_d/1263.

Specimen	U-DS	U-MS	T-DS	T-MS
Amplitude of global imperfection (mm)	3.4	4.0	3.3	5.0
Amplitude of global imperfection as a function of L_d	L_d/1860	L_d/1547	L_d/1911	L_d/1263

Table 12: Amplitudes of global imperfections in compression flanges

3.1.4 Measurements during tests

During tests, global displacements were recorded using steel wires at the web centre of four cross-sections spaced at L_d/6, as indicated in Figure 15. The twist rotation is also measured at the centre of the compression flange at the cross-section located at L_d/3 from the loaded section. The largest rotations and lateral displacements were expected to develop at this location.

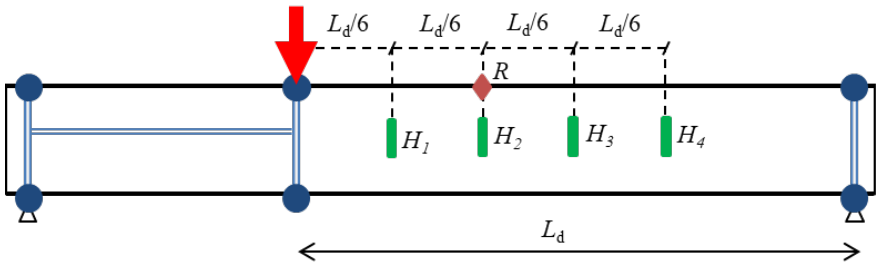

Figure 15: Global displacement and twist rotation measurements

Similarly, vertical displacements were measured at the locations indicated in Figure 16, i.e.:

- At the centre of the compression flange at both supports,
- At the centre of the tension flange of the loaded section, and
- At two intermediate positions located at $L_d/6$ and $L_d/3$ from the loaded section.

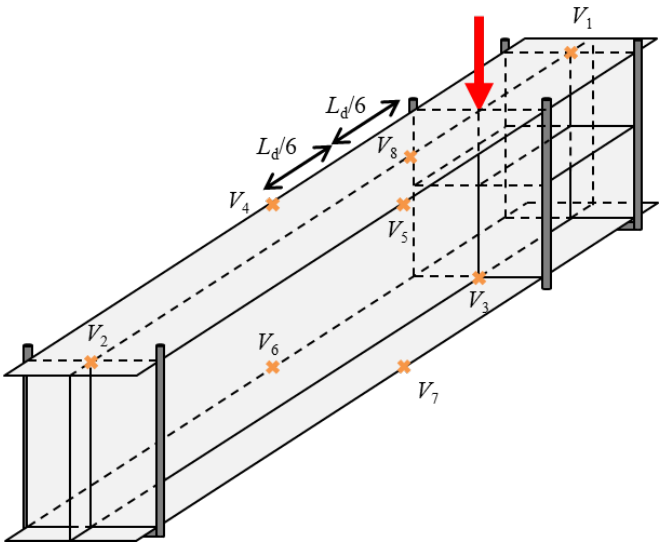

Figure 16: Vertical displacement measurements

The in-plane displacements of each flange tip and twist rotations are indeed recorded at the same location. The devices for displacement and twist rotation measurements are presented in Figure 17.

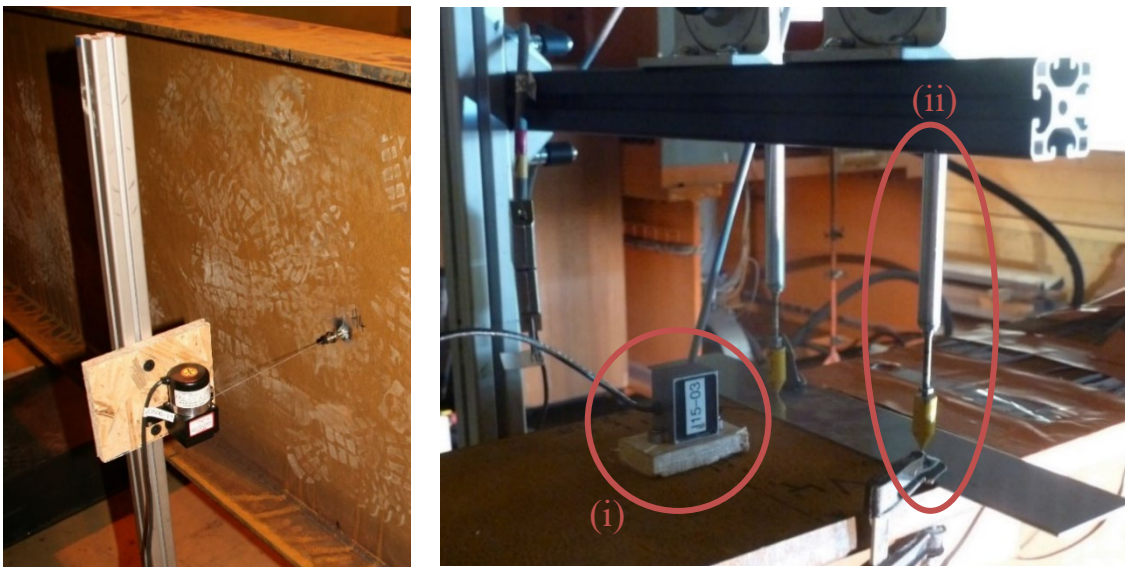

a) Global displacement b) Twist rotation (i) and vertical displacements (ii)

Figure 17: Means of measurements during the tests

Longitudinal strains were measured in three cross-sections. One was defined a priori as the critical one i.e. where the largest lateral displacements were expected according to numerical results. The

critical cross-section is located at 2.3 and 2.8 m from the loaded section for uniform and tapered beams, respectively. In addition, five strain gauges were positioned at two distinct cross-sections, located at $L_d/5$ from the critical one. The locations of the strain gauges are shown in Figure 18.

At the critical cross-section, nine strain gauges were pasted on the compression flange to study the progressive yielding. Three gauges were placed on the web and three on the tensile flange to quantify internal forces and bending moments.

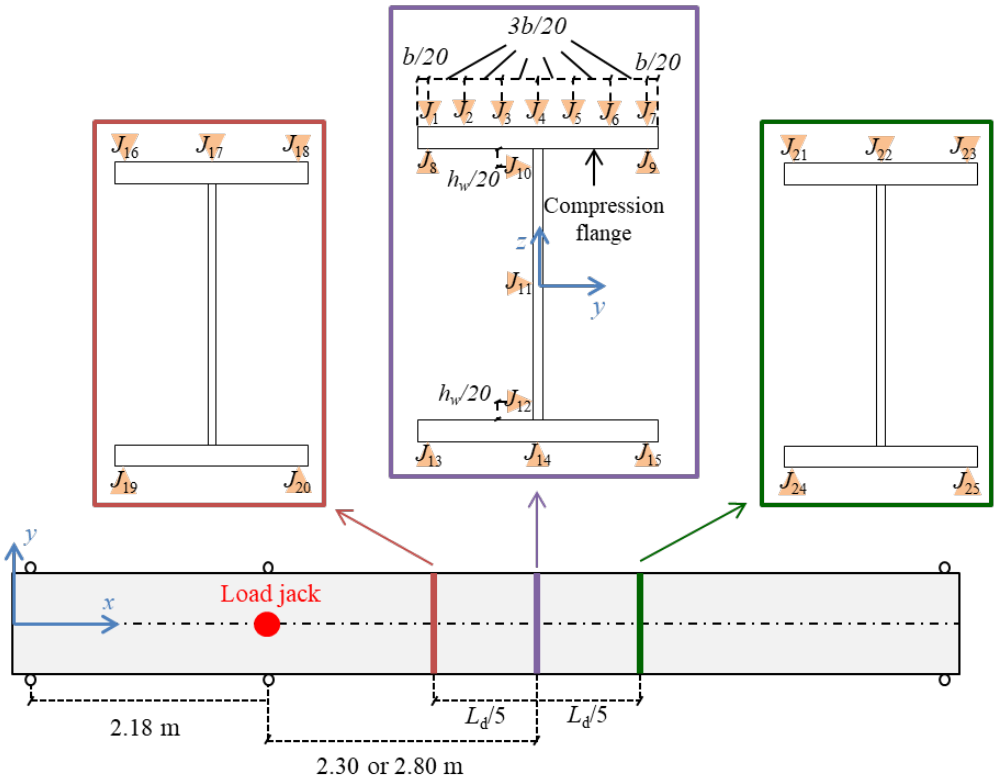

Figure 18: Location of strain gauges

3.1.5 Loading protocol

The loading protocol, described in Table 13, involved three steps. Both Steps A and B consist in cycles of loading and unloading with forces ranging from 40% to 100% of the ultimate limit state (ULS) design load. This load is computed according to the *General case* from EN 1993-1-1 [1] (see §6.3.2.2 of [1]), i.e. buckling curve *d*, with the nominal geometrical and mechanical properties. After a first step necessary for set-up and specimens readjustments and a second step to study the beams behaviour under the ULS design load, the specimens are loaded until failure in the final Step C.

Specimen	Step A	Step B	Step C
U-DS	0→154 kN→0 (×3)	0→269 kN→0→384 kN→0	0→Failure
U-MS	0→173 kN→0 (×3)	0→303 kN→0→433 kN→0	0→Failure
T-DS	0→163 kN→0 (×3)	0→285 kN→0→407 kN→0	0→Failure
T-MS	0→197 kN→0 (×3)	0→345 kN→0→493 kN→0	0→Failure

Table 13: Loading protocol

3.2 Experimental results

3.2.1 Overview

The failure mode of the four beams corresponds to lateral-torsional buckling depicted in Figure 19a) for specimen *T-MS*. Web distortion was also observed at post peak in specimen *U-MS*, as shown in Figure 19b).

The failure loads F_{ult} are given in Table 14 along with the elastic and plastic resistances of the loaded cross-section, labelled F_{el} and F_{pl}, respectively. The normalized slenderness and design loads of the specimens obtained using the *General case* from Eurocode 3 Part 1-1 [1] with the measured mechanical properties are also added. The *General case* requires the use of buckling curve *d*, with the corresponding ultimate load being labelled $F_{EC3,d}$. These values divided by the appropriate factor *f* accounting for the bending moment distribution, as described in §6.3.2.3 of [1], are also provided. For a triangular bending moment distribution, we get:

$$f = 1 - \frac{0.17}{1.33}\left[1 - 2.0\left(\overline{\lambda}_{LT} - 0.8\right)^2\right] \leq 1 \qquad (10)$$

where the normalized slenderness for lateral-torsional buckling is:

$$\overline{\lambda}_{LT} = \sqrt{\frac{M_{y,Rk}}{M_{y,cr}}} \qquad (11)$$

with:

$M_{y,rk}$: characteristic value of the member resistance to bending about the major axis,

$M_{y,cr}$: elastic critical lateral-torsional buckling bending moment resulting from a Linear Bifurcation Analysis (LBA).

568 Significant deviations are found between the experimental and Eurocode 3 [1] failure loads. The
569 differences range between 62% and 81% while the normalized slenderness range (0.74–0.93) is
570 representative of common practice.

Specimen	U-DS	U-MS	T-DS	T-MS
$\overline{\lambda}_{LT}$	0.830	0.736	0.927	0.809
F_{ult} (kN)	747.6	903.6	720.6	775.8
$F_{EC3,d}$ (kN)	450.8	499.9	428.7	479.5
$F_{EC3,d}/f$ (kN)	514.6	570.0	487.2	547.4
F_{el} (kN)	808.6	796.8	874.3	859.1
F_{pl} (kN)	940.2	1021.2	1021.2	1091.8

571 **Table 14: Design and experimental ultimate loads**

572 Explicitly accounting for the bending moment distribution increases the design loads but
573 experimental loads remain 42–58% greater. The substantial differences may be attributed to the
574 overly conservative design method making use of buckling curve *d*. Indeed, the failure load
575 obtained using the new verification format from prEurocode 3 Part 1-1 [20] for *U-DS* is equal to
576 658.8 kN. This value is only 12% lower than the experimental one and 46% higher than that
577 obtained using buckling curve *d* as currently prescribed. This new design method is restricted to
578 uniform and doubly symmetric beams, and thus design loads cannot be computed for the
579 remaining three specimens. The substantial deviations between the *General case* and the
580 experimental ultimate loads are also partly attributed to the flame-cuts that increase a member's
581 resistance against out-of-plane buckling (see [9], [16]) though this aspect is disregarded in
582 Eurocode 3.
583 Table 14 also highlights that the experimental ultimate load of beam *U-MS* is greater than its
584 cross-sectional characteristic resistance that corresponds to its elastic resistance. Indeed, *U-MS* is
585 a Class 3 beam in bending. For the remaining specimens, the ultimate load is 8–18% lower than
586 the elastic resistance of the loaded cross-section for two reasons. Firstly, the elastic resistance of
587 the loaded cross-section is greater than the characteristic resistance of the failure cross-section.
588 This result is attributed to the cross-sectional variation for tapered beams and to the Class 4 web

589 in pure bending of *U-DS*. Besides, in the range of normalized slenderness studied, the impact of
590 the member imperfections increases with the normalized slenderness. Specimen *U-MS* has the
591 lowest normalized slenderness, and thus its buckling behaviour is less affected by imperfections.

a) Lateral-torsional buckling of *T-MS* b) Post-peak web distortion of *U-MS*

592 **Figure 19: Failure of specimens tested**

593 A clear impact of the cross-sectional mono-symmetric design is noted, especially with uniform
594 beams. The ultimate load of *U-MS* is 20% greater than that of *U-DS*. The difference is reduced to
595 8% for tapered beams. The smaller difference between ultimate loads of tapered beams can be
596 attributed to distinct failure locations. Moreover, this deviation can be partly attributed to the
597 somewhat small yield strength measured in the compression flange of specimen *T-MS*, which is
598 more than 20 MPa lower than in the other 20-mm thick coupon tensile tests. Besides, the elastic
599 cross-sectional resistance slightly decreases as the thickness of the compression flange increases
600 owing to a lower value of f_y in thicker plates (see Table 8). The ultimate load of *T-DS* is only 4%
601 smaller than that of *U-DS* while the deviation between both mono-symmetric beams reaches 14%.
602 Again, the variation in the deviations can be attributed to different failure locations in the tapered
603 beams and the low yield strength measured in *T-MS*.

604 ### *3.2.2 Displacements and rotations*

605 The applied force is presented in Figure 20 as a function of load jack displacement. Initial stiffness
606 of specimens are close, although uniform beams are slightly stiffer than tapered ones. Mono-

607 symmetric beams also have greater stiffness than doubly symmetric ones. Differences are found
608 at post-peak, especially for *T-DS* exhibiting a sudden 100-kN decrease which may correspond to
609 an elastic equilibrium bifurcation.

610 Force–displacement and force–rotation curves measured by H_2 and R are presented in Figure 21a)
611 and Figure 21b), respectively. The results are presented considering the same buckling direction
612 for all tests. Global displacements and twist rotations are very small to negligible during loading,
613 while in the last loading interval 50–100 kN before the peak load, a visible increase is initiated.
614 During the unloading stage, displacements and rotations increase significantly with barely any
615 variable stiffness. However, the post-peak slope of the twist rotation measured in *U-MS* fluctuates,
616 which might be associated with the post-peak web distortion observed for this specimen only.

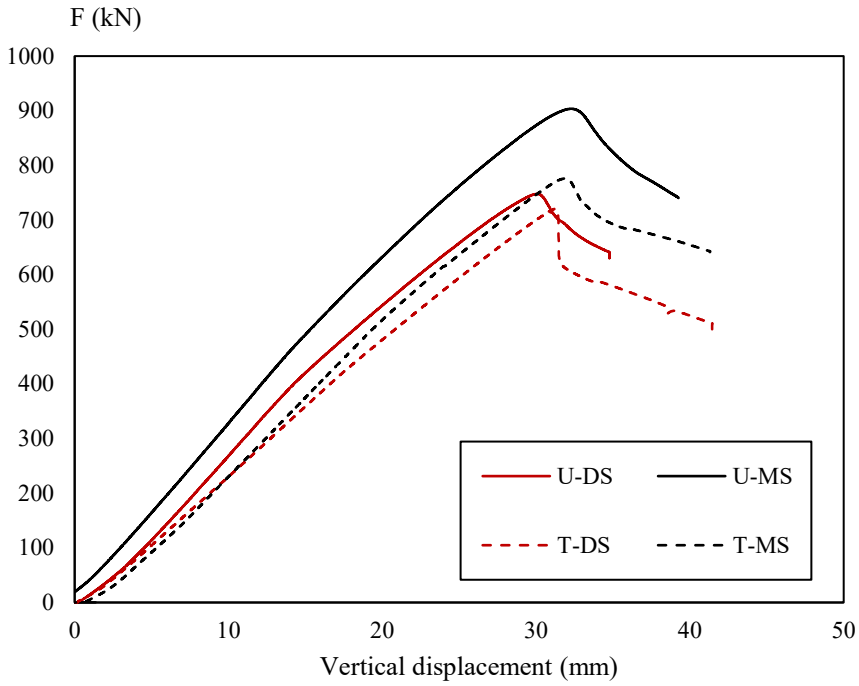

617

618 **Figure 20: Force–vertical displacement of the load jack**

619 The equilibrium bifurcation suggested for specimen *T-DS* is supported by results presented in
620 Figure 21. Indeed, the global displacements show a quasi-infinite initial stiffness until almost the
621 failure load with a changing in the sign. A clear transition is observed before the ultimate load in
622 the other tests. The twist rotation measured in *T-DS* exhibits the greatest initial stiffness with a
623 brief transition between pre and post-peak behaviours.

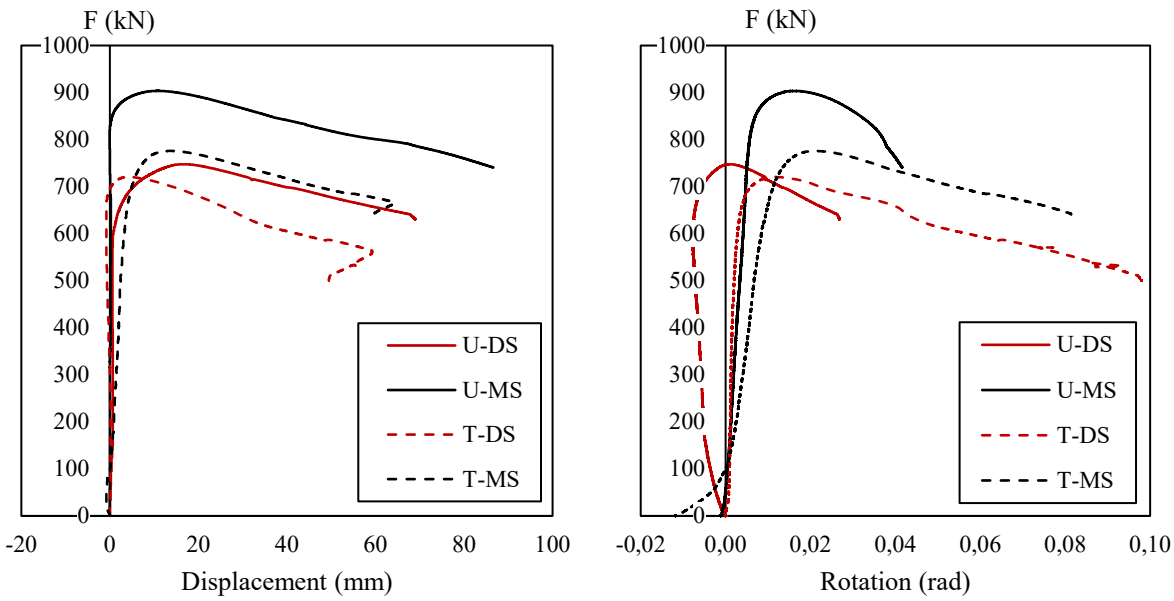

a) Global displacement (H_2) b) Twist rotation (R)

Figure 21: Force–displacement and rotation curves

The global displacements u measured at positions H_1 to H_4 are presented in Figure 22 for three key levels of loading level:

- 85% of the ultimate load during loading,
- The ultimate load,
- 90% of the ultimate load during unloading.

The global displacements at failure can be approximated by half sine-waves with maximum values close to H_2 for uniform beams. The failure cross-section is closer to the smallest end section in the tapered beams owing to the cross-section variations. As a result, the maximum displacements in tapered beams are close to H_3, located at mid-span. The bucking shapes are similar under the ultimate load and during unloading. Small differences are observed for the displacements measured at H_3 in *U-MS* and H_1 in *T-DS* owing to pre-buckling displacements.

The buckling shapes exhibit similar magnitudes for all tests except for *T-DS*. Maximum displacements of approximately 15 and 50 mm are seen under the ultimate load and during unloading, respectively. Owing to a change in the sign of the global displacements as buckling is initiated, the global displacements of *T-DS* are much smaller. The magnitude of the buckling shapes in *T-DS* are approximately half the magnitudes of the buckling shapes in the other three specimens.

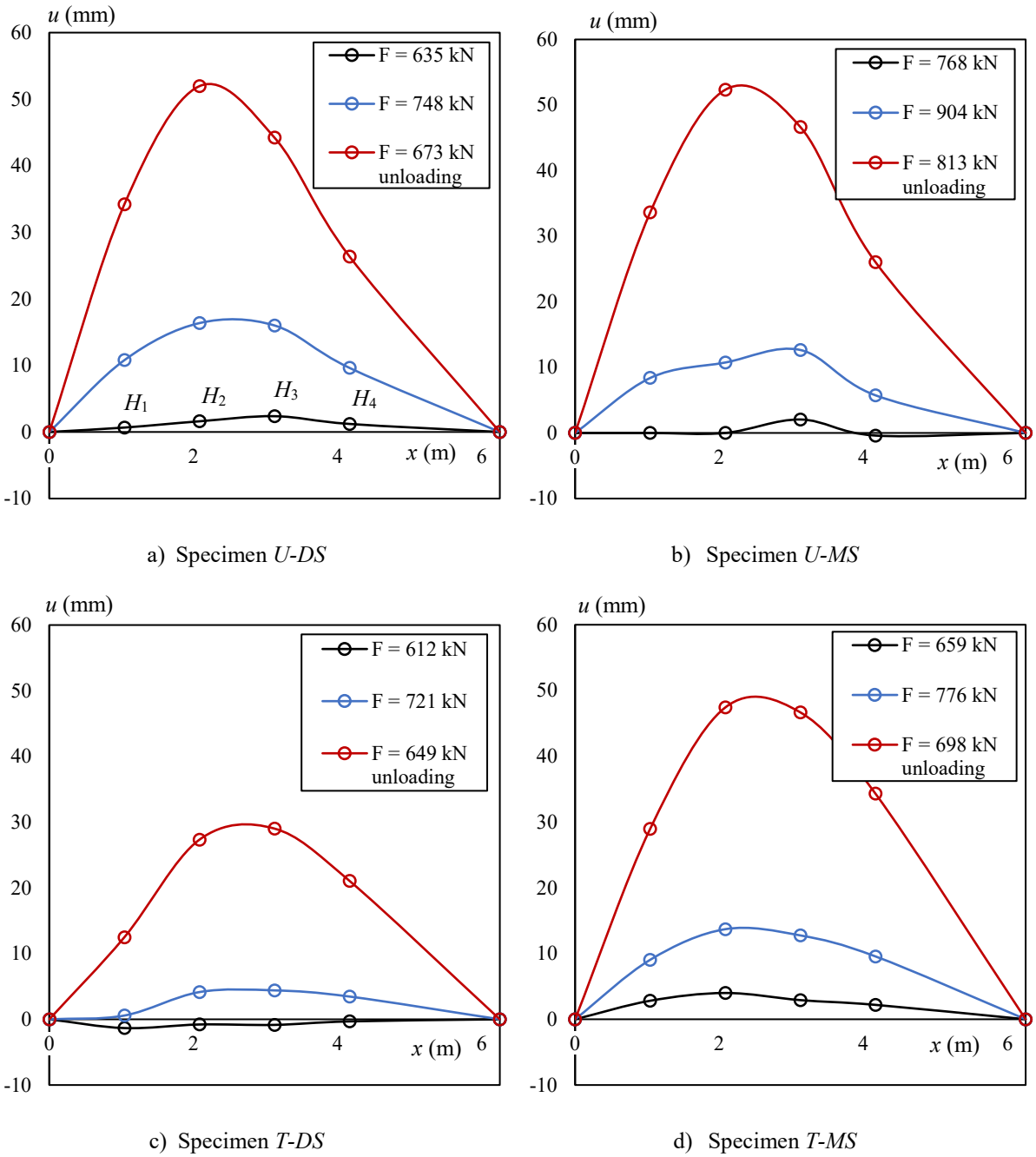

Figure 22: Global displacements distributions

3.2.3 *Strains*

The distributions of uniaxial strains measured in the compression flange of the critical cross-section are displayed in Figure 23, again under:

- 85% of the ultimate load during loading,
- The ultimate load,
- 90% of the ultimate load during unloading.

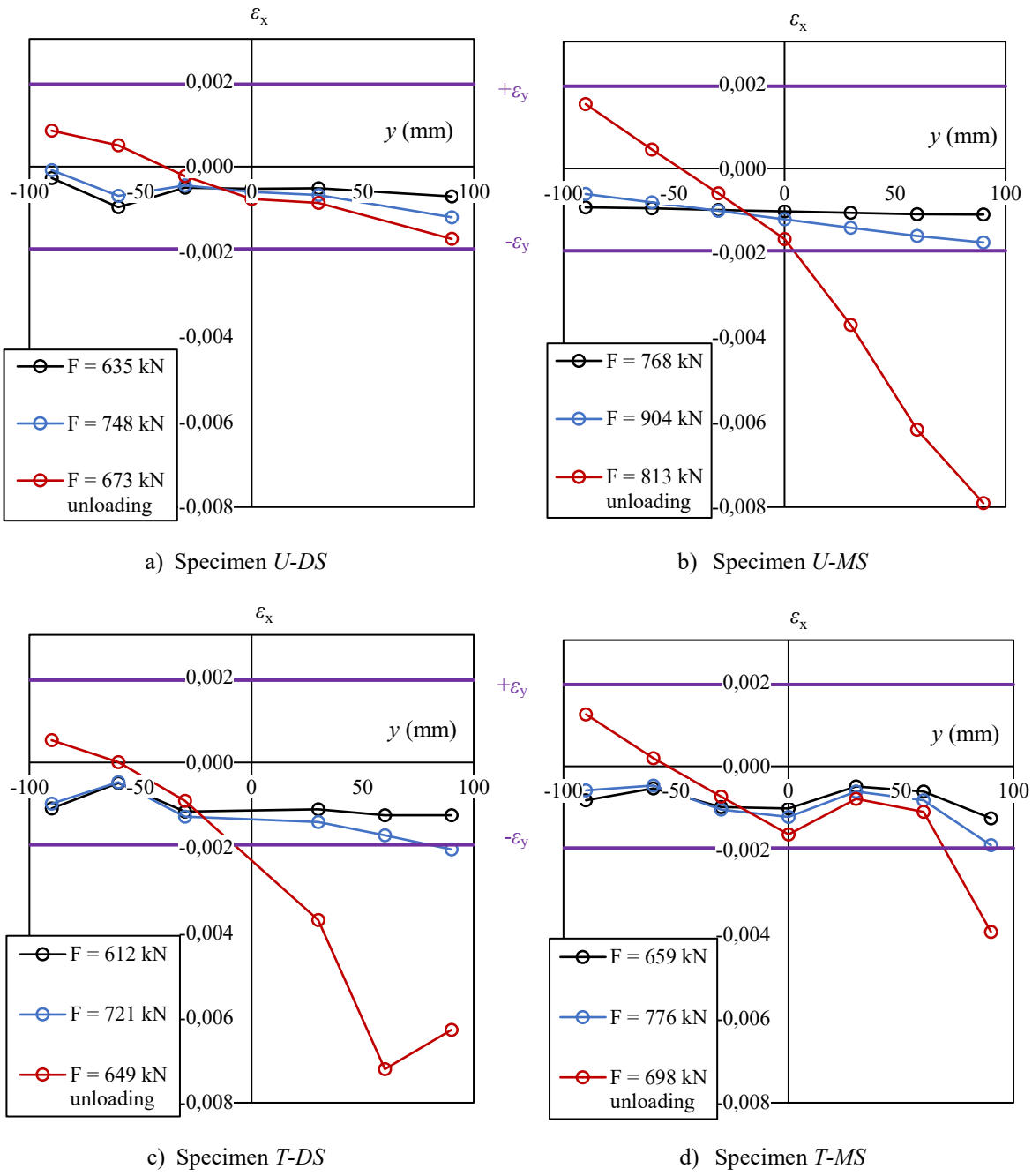

a) Specimen *U-DS*

b) Specimen *U-MS*

c) Specimen *T-DS*

d) Specimen *T-MS*

649 **Figure 23: Axial strains in compression flanges of the critical cross-sections**

650 The yield strains $\varepsilon_y = f_y/E$ are added for comparison. The strains distribution is almost uniform
651 along the flange width before lateral-torsional buckling. At failure, the magnitude of the
652 compressive strains increases at one flange tip while decreasing at the other. This effect intensifies
653 during post-peak leading to tensile strains at one tip and significant compressive strains at the
654 other end. When the ultimate resistance is reached, the magnitudes of the largest compressive
655 strains are very close in all specimens except *U-DS*. They are approximately equal to 0.002, which

is close to ε_y. A lower value of approximately 0.0012 is found for specimen *U-DS*. Lateral-torsional buckling is observed between the elastic and inelastic regimes for all specimens except *U-DS*, which failed in the elastic range.

3.3 Conclusions on lateral-torsional buckling tests

A scarcity of experimental tests on the stability of welded members with a mono-symmetric and/or tapered slender cross-section motivated the present experimental study. This study was conducted to better understand the actual buckling behaviour of welded beams made of flame-cut flanges made of regular steel grade. Four S355 beams were tested: two uniform and two tapered. For both groups of specimens, there was one with a doubly symmetric and one with a mono-symmetric cross-section. Experimental lateral-torsional buckling occurred in the elastic regime for the uniform doubly symmetric specimen and at the frontier with the inelastic regime in the other three tests. The prescriptions of the current Eurocode 3 [1] that make use of buckling curve *d* proved to be overly conservative. The new verification format of prEurocode 3 [20] provides a more accurate ultimate resistance for the uniform doubly symmetric beam. However, this design method is restricted to uniform doubly symmetric beams. A substantial part of the buckling resistance margin may also be attributed to the beneficial effect of the flame-cuts made at the flange tips, which are not considered in the code.

4 NUMERICAL MODEL

4.1 Finite element model

As an alternative to experimental tests, GMNIA-type computations are employed to evaluate the resistance of a welded member subjected to a bending moment distribution. These Geometrically and Materially Non-linear Analyses account for the geometrical and material Imperfections of the members, producing numerous reference results at a reduced cost when compared to large-scale tests. A numerical model is therefore presented hereafter. The previously described lateral-torsional buckling tests are modelled using 4-noded shell finite elements (SHELL 181) with ANSYS v.2020 software. Each node possesses 6 degrees of freedom while 5 integration points are defined through the thickness. The shell elements account for the change in thickness during non-linear analyses. Accordingly, the measured material laws are integrated into the numerical model with modifications to represent the accurate true stress – true strain behaviour using the prescriptions of Eurocode 3 Part 1-5 [24] and prEurocode 3 Part 1-14 [25] (see Figure 24):

$$\sigma_{\text{true}} = \sigma\left(1+\varepsilon\right) \tag{12}$$

$$\varepsilon_{\text{true}} = \ln\left(1+\varepsilon\right) \tag{13}$$

where σ is the engineering stress and ε the engineering strain.

Residual stresses are introduced based on the distributions measured in specimens *Wfc_200-15* for both doubly symmetric beams and in *Wfc_200-15/20* for both mono-symmetric beams. The experimental values are averaged to present a symmetry about the flanges and web centres. The distributions inserted in the numerical analyses are shown in Figure 25.

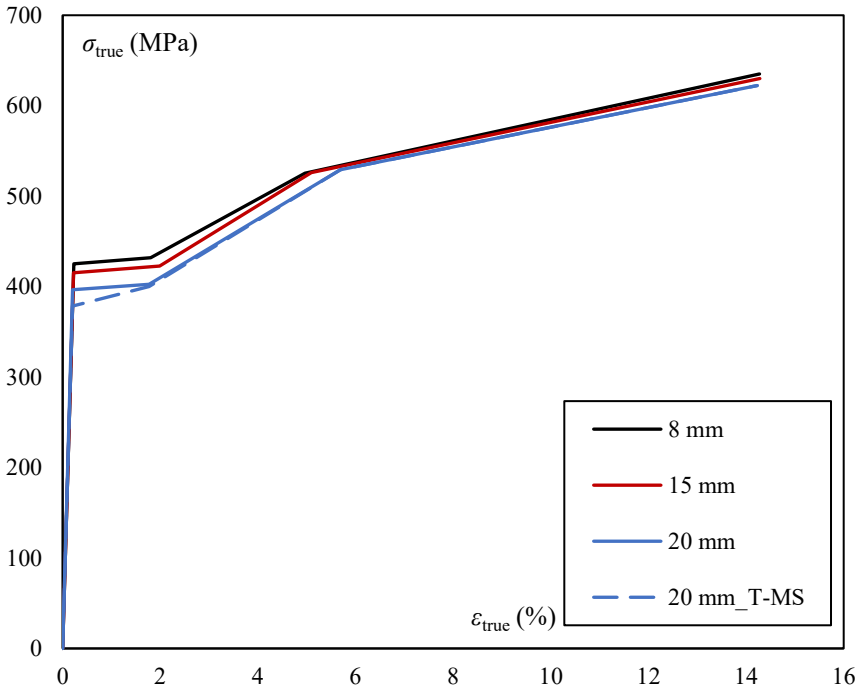

692

693 **Figure 24: Stress-strain curves used in the FE analyses**

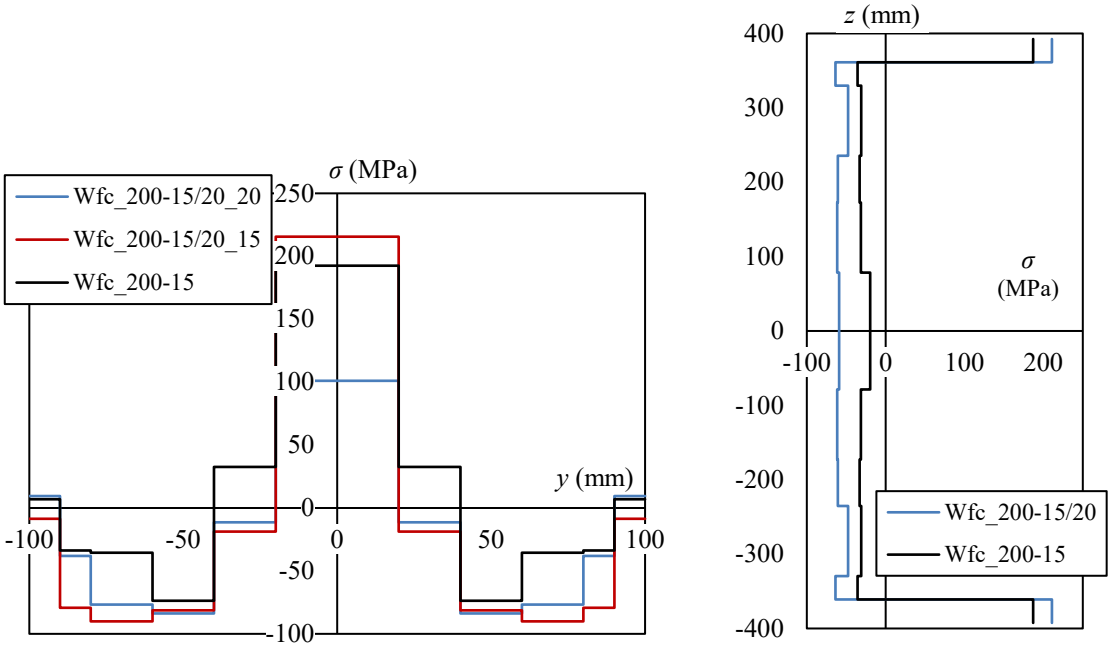

a) Flanges b) Web

694 **Figure 25: Residual stresses used in the FE analyses**

695 Geometrical global and local plate imperfections are also introduced using the magnitudes
696 presented in Table 11 and Table 12. The shape of the global imperfection is homothetic to the
697 elastic critical buckling mode obtained using LBA-type calculations, as recommended by
698 Boissonnade et al. [35] and Couto et al. [36]. Local imperfections are represented using half-sine

699 waves introduced in both directions of the web and flanges. As recommended by Gérard et al.[37],
700 local imperfections in the flanges and web have similar periods and their amplitudes are similar
701 with respect to the plate width.

702 At both supports, the vertical displacement of the bottom flange is prevented. The lateral
703 displacement of the free ends of the transverse stiffeners is also fully restrained on both sides of
704 the web. To prevent any rigid body motion, the longitudinal displacement is fixed at the centre of
705 the bottom flange of the left support.

706 *4.2 Comparison with experimental tests*

707 The numerical ultimate resistances are presented in Table 15 for the four tests and compared with
708 experimental values. The results are in very good agreement, with the maximum deviation being
709 1.7%, except for *T-MS* where a greater difference of 5.6% is obtained, which is still acceptable.

Specimen	U-DS	U-MS	T-DS	T-MS
F_{GMNIA} (kN)	753.6	898.4	708.1	819.6
$F_{experimental}$ (kN)	747.6	903.6	720.6	775.8
$F_{GMNIA}/F_{experimental}$	1.008	0.994	0.983	1.056

710 **Table 15: Numerical and experimental ultimate resistances**

711 Figure 26 presents the experimental and numerical buckled shapes of specimen *U-MS* under
712 ultimate load. Both exhibit a clear lateral displacement of the compression flange. The numerical
713 von Mises stresses depicted in Figure 26b) are maximal in the vicinity of the loaded section while
714 the maximal displacements are observed close to mid-span. This observation is due to the
715 triangular bending moment distribution that reaches its peak value at the loaded section while the
716 second order out-of-plane bending moment M_z^{II} and bimoment B^{II} are maximal near mid-span.

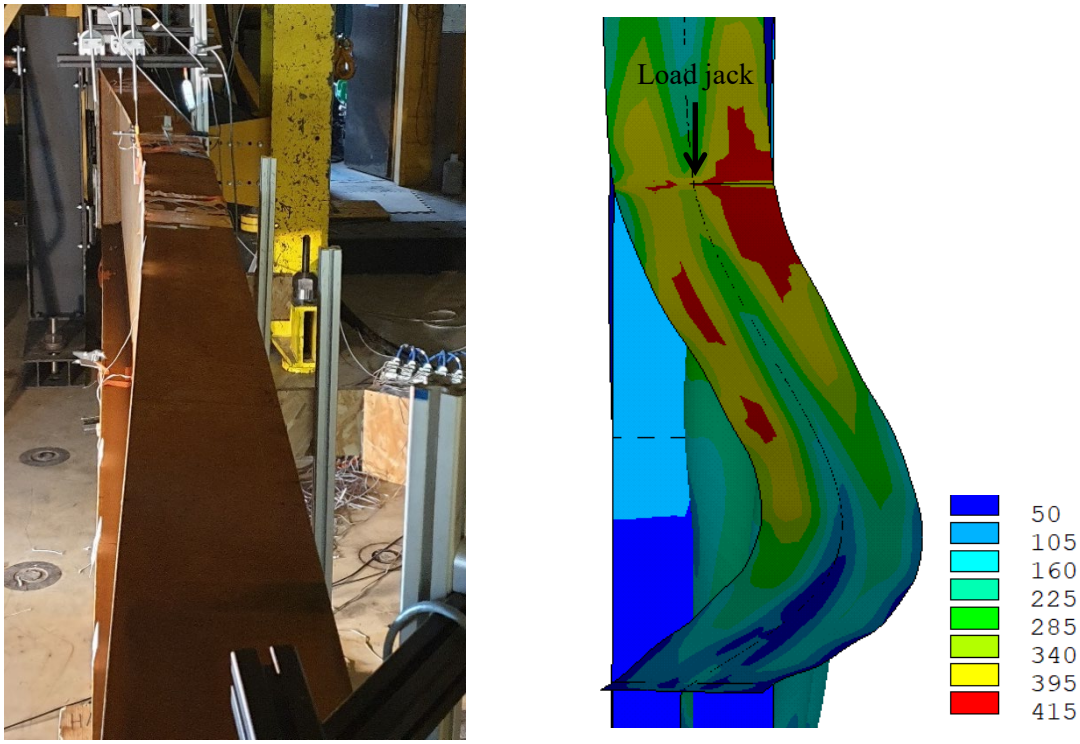

a) Experimental b) Numerical von Mises Stresses (N/mm²)

Figure 26: Buckled shape of specimen *U-MS* under ultimate load

The force–vertical displacement curves of the load jack are presented in Figure 27. Numerical and experimental curves are in very good agreement; the initial and post-peak stiffness are very close. The evolution of the numerical and experimental global displacements measured at H_2 and H_3 (see Figure 15) are presented in Figure 28.

The force–displacement curves are in good agreement, although slight differences can be observed for *U-MS*. The numerical initial stiffness is slightly greater than the experimental one for H_2 and post-peak slopes are also slightly different for both H_2 and H_3. Differences are also observed for *T-DS* owing to the changing of the global displacements sign at the end of the loading stage.

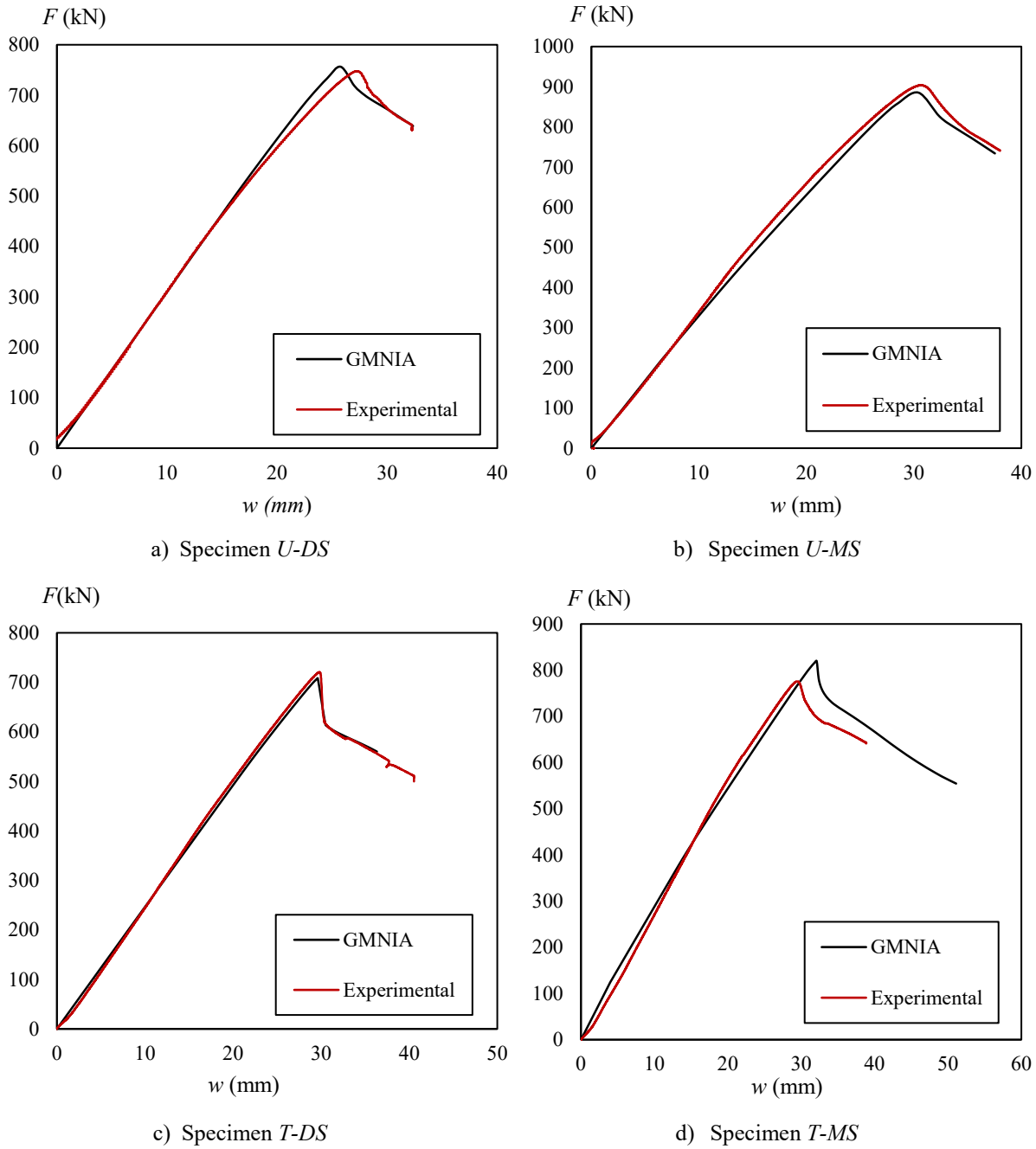

Figure 27: Force–vertical displacement curves: Experimental and numerical results

The experimental tests performed by Tankova [18], Schaper et al. [19] and Ji et al. [21]-[22] for welded I-section members made of flame-cut flanges failing owing to out-of-plane buckling are also modelled for comparison. The experimental and numerical failure loads are compared in Table 16. The numerical results are obtained using the residual stress model from Figure 10. Geometrical global imperfections are introduced scaled to the critical buckling mode shape with the measured amplitudes. A lack of experimental data is noticed regarding local imperfections. Thus, local imperfections are inserted following the prescriptions of Eurocode 3 Part 1-5 [24] and

735 prEurocode 3 Part 1-14 [25], i.e. using half-sine waves in the flanges and web. The amplitudes of
736 the local imperfections are 70% of $h_w/200$ in the web and 70% of $b/200$ in the flanges. Small
737 deviations are noted which can be partly attributed to the residual stress model which slightly
738 differs from the distributions measured as part of each experimental study.

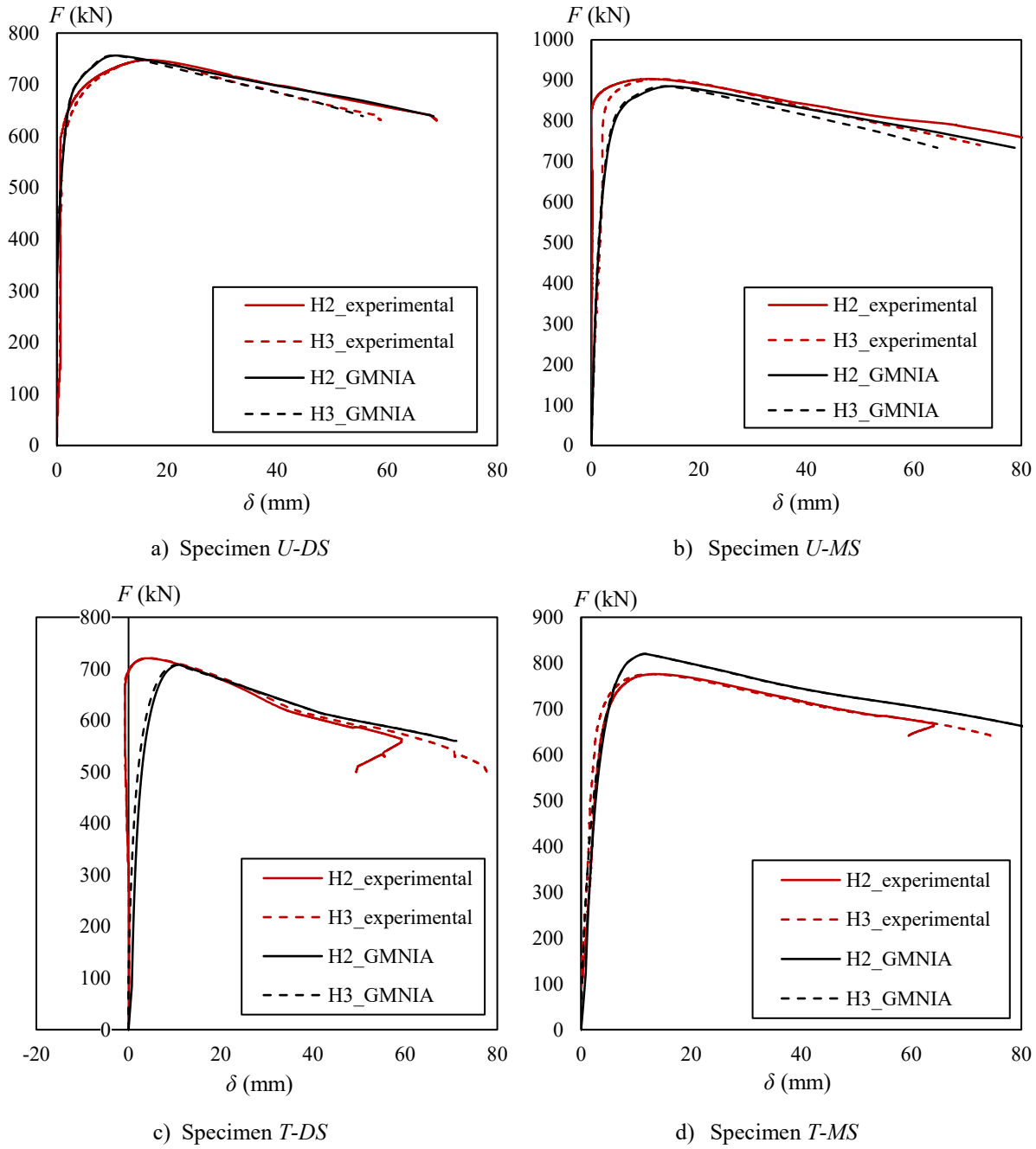

a) Specimen *U-DS* b) Specimen *U-MS*

c) Specimen *T-DS* d) Specimen *T-MS*

739 **Figure 28: Force–global displacement curves: Experimental and numerical results**

740 The comparison between experimental and numerical failure load from the present study as well
741 as the experimental tests campaigns of Tankova [18], Schaper et al. [19] and Ji et al. [21]-[22]
742 show that they match very well. The same applies for the displacements measured in the present

743 study. Although some differences can be seen, they remain acceptable and the numerical model
744 may be used to perform a large number of GMNIA-type calculations. In Section 5, the tested
745 specimens presented in Section 3 are analysed with different residual stress models and
746 normalized slenderness.

Reference	Specimen	F_{GMNIA}/F_{Exp}
Tankova [18]	C1	1.009
	C2	0.986
	B1	1.000
	B2	1.029
	BC	1.028
Schaper et al. [19]	Pos. 1	0.987
	Pos. 1f$_y$	0.944
	Pos. 3-1	1.044
	Pos. 3-1f$_y$	0.915
	Pos. 3-2	0.984
	Pos. 4-1	0.972
	Pos. 5	1.062
	Pos. 14	1.078
Ji et al. [21]-[22]	G6-430-32-1-f	0.906

747 **Table 16: GMNIA and Experimental ultimate loads**
748

5 INFLUENCE OF THE FLANGE FABRICATION PROCESS

5.1 Impact on the test specimens

Additional numerical analyses are performed considering the model described in sub-section 4.1 with alternative residual stress distributions. Instead of those shown in Figure 25, different residual stress models are considered:

- No residual stress (labelled *ØRS*),
- The residual stresses distributions measured in the welded members with hot-rolled flanges (see Figure 29) (*Exp-hr*),
- The residual stress model for welded members made of hot-rolled flanges prescribed by prEurocode 3 Part 1-14 [25] (see Figure 1) (*MOD-hr*),
- The new residual stress model for welded members made of flame-cut flanges (see Figure 10) (*MOD -fc*).

The ultimate resistances calculated numerically are compared in Table 17 with experimental results but also with numerical results obtained using the measured distributions, defined as numerical reference values. The numerical model that disregards residual stresses yields 3–6% greater ultimate loads than the numerical reference values. The difference is reduced when compared to the experimental results, except for specimen *T-MS* where a 12% deviation is noted. Integrating the residual stresses measured in welded members made of hot-rolled flanges yields ultimate resistances 3–5% lower than using the measurements in welded beams made of flame-cut flanges. The deviation from experimental results is larger except for *T-MS* for which the numerical result is 1% greater than the experimental result.

Using the new residual stress model for welded members made of flame-cut flanges produces numerical results 4–6% lower than the numerical reference values. These numerical results lie closer to the experimental values, except for *T-DS* that exhibits a 7% deviation. Implementing the residual stress model for welded members made of hot-rolled flanges [25] produces ultimate loads approximately 14% lower than the numerical reference values. The deviations with the experimental results fluctuate more, ranging from 9% to 16%.

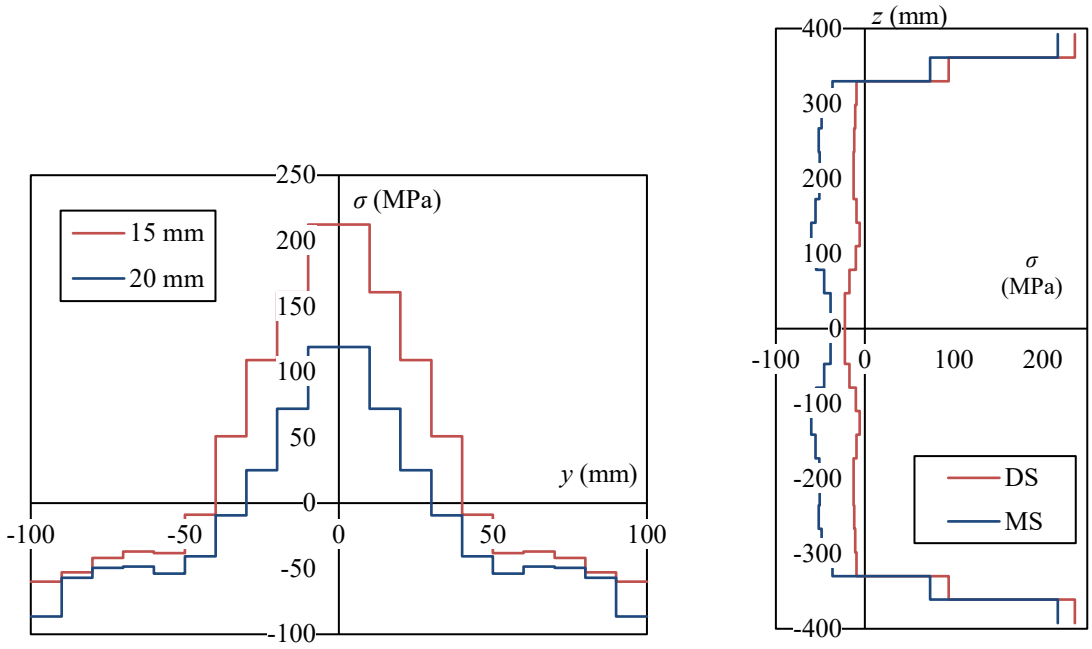

a) Flanges b) Web

Figure 29: Residual stresses used in the FE analyses for welded beams made of hot-rolled flanges

For welded beams made of hot-rolled flanges, the use of the model from prEN 1993-1-14 [25] proves to be overly conservative when compared with the experimental distributions. The deviations range between 10% and 12%. Finally, a 10% difference is seen between the numerical results using both residual stress models.

Reference value	Ratio	U-DS	U-MS	T-DS	T-MS
Numerical calibrated model	$F_{FEA,ØRS}/F_{FEA,Measured}$	1.031	1.029	1.037	1.063
	$F_{FEA,Exp\text{-}hr}/F_{FEA,Measured}$	0.957	0.969	0.949	0.961
	$F_{FEA,MOD\text{-}hr}/F_{FEA,Measured}$	0.860	0.860	0.855	0.860
	$F_{FEA,MOD\text{-}fc}/F_{FEA,Measured}$	0.965	0.961	0.950	0.943
Experimental tests	$F_{FEA,ØRS}/F_{Experimental}$	1.039	1.023	1.019	1.123
	$F_{FEA,Exp\text{-}hr}/F_{Experimental}$	0.964	0.963	0.933	1.015
	$F_{FEA,MOD\text{-}hr}/F_{Experimental}$	0.867	0.855	0.841	0.909
	$F_{FEA,MOD\text{-}fc}/F_{Experimental}$	0.972	0.955	0.933	0.997

Table 17: Numerical ultimate resistances for different residual stress models

5.2 Sensitivity analyses

Further GMNIA-type computations are performed considering the uniform doubly symmetric beam but under a constant bending moment and varying the normalized slenderness. To evaluate

the impact of the flange fabrication process on the ultimate bending moment, the residual stress models for welded beams made of hot-rolled [25] and flame-cut flanges are used in turn (see Figure 1 and Figure 10, respectively). Numerical analyses are also conducted in which the residual stresses are disregarded.

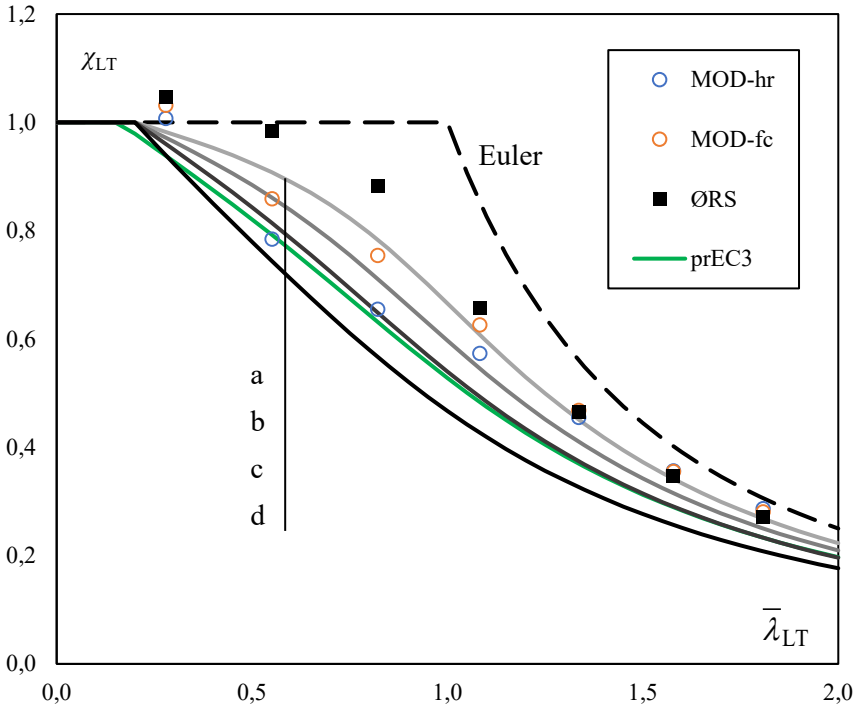

Figure 30: Numerical results for *U-DS* under a constant bending moment

Results are presented in Figure 30 along with the four buckling curves *a* to *d* and that from the new verification format in prEN1993-1-1 [20] for *U-DS*. A significant influence of the residual stress model is noted, especially for intermediate slenderness. Accounting for the flame-cuts increases substantially the ultimate bending moment by up to 15%. In the least favourable case, numerical results for welded beams made of flame-cut flanges are obtained with buckling curve *b* while both EN 1993-1-1 [1] and prEN1993-1-1 [20] require the use of buckling curve *d* for the studied beam, whatever the flange type. The deviation is reduced when compared with the buckling curve from the new verification format that is close to curve *c*. For hot-rolled flanges, the lowest results lie between buckling curves *c* and *d*, for low to intermediate slenderness. For high slenderness, results are similar whatever the flange type i.e. the imperfection effect on the resistance to buckling diminishes. Since significant deviations are highlighted, distinct methods should exist for welded members made of hot-rolled or flame-cut flanges.

6 CONCLUSIONS

Existing residual stress models for welded I-members made of hot-rolled or flame-cut flanges were first described. Few models rely on a strong experimental basis, which generally consist in stocky specimens with a lack of results for commonly slender cross-sections. Thus, residual stresses of eight S355 slender cross-sections with flanges of varying width, thickness, and fabrication process were measured. Experimental results confirmed a significant impact of the flame-cuts on the residual stress distributions. Tensile stresses were generally found at the ends of flame-cut flanges that also feature low-magnitude compressive stresses. Considering differences existing between models and experimental distributions, a new model is proposed for welded members made of flame-cut flanges with $f_y \leq 460$ MPa. It is based on experimental data from the present work and extracted from the literature ([5], [10], [19], [23] and [33]). This model depends on the ratios b/t_f and h_i/b and can be employed for doubly or mono-symmetric members. Past lateral-torsional buckling tests on welded beams made of flame-cut flanges focused on stocky doubly symmetric cross-sections. Experimental data for mono-symmetric and/or tapered commonly slender cross-sections are missing, requiring lateral-torsional buckling tests on these configurations. Thus four S355 slender tapered or uniform (doubly or mono-symmetric cross-section) beams have been tested. The EN 1993-1-1 [1] rules revealed overly conservative, yielding ultimate loads 62 to 81% lower than experimental ones. The deviation is reduced to 12% for *U-DS* when using the new method suggested in prEN 1993-1-1 [20] which is restricted to uniform doubly symmetric beams.

Shell finite elements were then used to model the tests considering the measured material characteristics, residual stresses and geometrical imperfections amplitudes, with the shapes suggested in [24]-[25]. Numerical and experimental results are in very good agreement with a maximal 5.6%-deviation between ultimate loads. Alternatively, residual stress models for welded beams with hot-rolled or flame-cut flanges were employed, yielding an average 10%-deviation. The difference increased up to 15% for *U-DS* under a constant bending moment. These substantial deviations confirm the relevance of adopting a specific design method for flame-cut flanges.

7 REFERENCES

[1] CEN. (2005) *EN 1993-1-1: Eurocode 3 – Design of steel structures – Part 1-1: General rules and rules for buildings*. European Committee for Standardization.

[2] ECCS, Committee 8 – Stability. (1976) *Publication n°22: Manual on stability of steel structures*.

[3] Cranston, W. (1967) *Thesis for the degree of Master of Science: The strength of heavy welded shapes*. Lehigh University, Bethlehem, Pennsylvania, USA.

[4] Alpsten, G.; Tall, L. (1969) *Fritz laboratory Report No. 337.12: Residual stresses in heavy welded shapes*. Lehigh University, Bethlehem, Pennsylvania, USA.

[5] Schaper, L.; Tankova, T.; Simões da Silva, L.; Knobloch, M. (2022) *A novel residual stress model for welded I-sections*. Journal of Constructional Steel Research, vol. 188, 107017.

[6] Barth, K.; White, D. (1998) *Finite element evaluation of pier moment-rotation characteristics in continuous-span steel I girders*. Engineering Structures, vol. 20, n°8, pp 761-778.

[7] Chacón, R.; Mirambell, E.; Real, E. (2009) *Influence of designer-assumed initial conditions on the numerical modelling of steel plate girders subjected to patch loading*. Thin-Walled Structures, vol. 47, pp 391-402.

[8] Wang, Y.; Li, G.; Chen, S. (2012) *Residual stresses in welded flame-cut high strength steel H-sections*. Journal of Constructional Steel Research, vol. 79, pp 159-165.

[9] Thiébaud, R. (2014) *Résistance au déversement des poutres métalliques de pont*. PhD thesis, Ecole polytechnique fédérale de Lausanne, Switzerland.

[10] Yang, B.; Nie, S.; Kang, S.; Xiong, G.; Hu, Y.; Bai, J.; Zhang, W.; Dai, G. (2017) *Residual stress measurements on welded Q345GJ steel H-sections by sectioning*

method and method improvement. Advanced Steel Construction, vol. 13, n°1, pp 78-95.

[11] Unsworth, D.; Driver, R.; Li, L.; Twizell, S.; Imanpour, A. (2021) *Characterization of residual stresses for LTB simulations of modern welded girders*. Journal of Constructional Steel Research, vol. 183, 106769

[12] Ban, H.Y.; Shi, G.; Bai, Y.; Shi, Y.J.; Wang, Y. (2013) *Residual stress of 460 MPa high strength steel welded I section: Experimental investigation and modelling*. International Journal of Steel Structures, vol. 13, n°4, pp 691-705.

[13] Taras, A. (2010) *Contribution to the development of consistent stability design rules for steel members*. PhD thesis, Technical University of Graz, Austria.

[14] Simões da Silva, L.; Marques, L.; Rebelo, C. (2010) *Numerical validation of the General method in EC3-1-1 for prismatic members*. Journal of Constructional Steel Research, vol. 66, pp 670-679.

[15] Marques, L. (2012) *Tapered steel members: flexural and lateral-torsional buckling*. PhD thesis, Universidade de Coimbra, Portugal.

[16] Prawel, S.; Lee, G. (1974) *Bending and buckling strength of tapered structural members*. Welding Research Supplement, vol. 1, pp 75-84.

[17] ESCS Steel RTD Programme (2001) *Lateral-torsional buckling in steel and composite beams: Testing of 4 tapered steel beams*. Université de Liège, Belgium.

[18] Tankova, T. (2018) *Stability design of columns, beams and beam-columns: behaviour, general formulation and reliability*. PhD thesis, Universidade de Coimbra, Portugal.

[19] Schaper, L.; Jörg, F.; Winkler, R.; Kuhlmann, U.; Knobloch, M. (2019) *The simplified method of the equivalent compression flange*. Steel Construction, vol. 12, n°4, pp 264-277.

[20] CEN/TC 250. (2021) *prEN 1993-1-1: Eurocode 3 – Design of steel structures – Part 1-1: General rules and rules for buildings*. CEN/TC 250/SC 3/WG 1 – Draft version.

[21] Ji, X.L.D.; Driver, R. Imanpour, A. (2019) *Large-scale lateral-torsional buckling tests of welded girders*. Steel Centre Engineering Report n°15, University of Alberta, Canada.

[22] Ji, X.L.D.; Twizell, S; Driver, R.; Imanpour, A. (2022) *Lateral Torsional Buckling Response of Compact I-Shaped Welded Steel Girders*. Journal of Structural Engineering, vol. 148, n°10, 04022149.

[23] Unsworth, D.; Driver, R.; Li, L. (2020) *Measurement and prediction of residual stresses in welded girders*. Journal of Constructional Steel Research, vol. 169, 106007.

[24] CEN. (2007) *EN 1993-1-5: Eurocode 3 – Design of steel structures – Part 1-5: Plated structural elements*. European Committee for Standardization.

[25] CEN/TC 250. (2021) *prEN 1993-1-14: Eurocode 3 – Design of steel structures – Part 1-14: Design assisted by finite element analysis*. CEN/TC 250/SC 3 – prEN 1993-1-14 – Draft version.

[26] ECCS, Technical Committee 8 – Structural stability (1984) *Publication n°33: Ultimate limit state calculation of sway frames with rigid joints*.

[27] *Swedish Regulations for Steel Strutures, BSK 99* (2003) National Board of Housing, Building and Planning.

[28] Gozzi, J. (2007) *Patch Loading Resistance of Plated Girders – Ultimate and serviceability limit state*. PhD thesis, Luleå University of Technology, Sweden.

[29] Trahair, N. (2012) *Inelastic buckling design of monosymmetric I-beams*. Engineering Structures, vol. 34, pp 564-571.

[30] Kabir, I.; Bhowmick, A. (2018) *Applicability of North American standards for lateral torsional buckling of welded I-beams*. Journal of Constructional Steel Research, vol. 147, pp 16-26.

[31] Kim, Y. (2010) *Behaviour and design of metal building frames using general prismatic and web-tapered steel I-section members*. PhD thesis, Georgia Institute of Technology, Atlanta, USA.

[32] Liu, X. (2017) *Structural effects of welding onto high strength S690 steel plates and welded sections*. PhD thesis, The Hong Kong Polytechnic University.

[33] Tankova, T. Simões da Silva, L.; Balakrishnam, M.; Rodrigues, D.; Launert, B.; Pasternak, H.; Yadanar Tun, T. (2019) *Residual stresses in welded I-section steel members*. Engineering structures, vol. 197, 103398

[34] CEN. (2018) *EN 1090-2: Execution of steel and aluminium structures – Part 2: Technical requirements for steel structures*. European Committee for Standardization.

[35] Boissonnade, N.; Somja, H. (2012) *Influence of Imperfections in FEM Modeling of Lateral Torsional Buckling*. Proceedings of the Annual Stability Conference – Structural Stability Research Council, Grapevine, USA.

[36] Couto, C.; Vila Real, P. (2019) *Numerical investigation on the influence of imperfections in the lateral-torsional buckling of beams with slender I-shaped welded sections*. Thin-Walled Structures, vol. 145, 106429

[37] Gérard, L.; Li, L.; Kettler, M.; Boissonnade, N. (2019) *Recommendations on the geometrical imperfections definition for the resistance of I-sections*. Journal of Constructional Steel Research, vol. 162, 105716.

831